The role of brucite in water and element cycling during serpentinite subduction – Insights from Erro Tobbio (Liguria, Italy)

Daniel Peters[1,2,3], Thomas Pettke[1], Timm John[4], and Marco Scambelluri[5]

[1] University of Bern, Institute of Geological Sciences, Baltzerstrasse 1+3, 3012 Bern, Switzerland

[2] Institute de Recherche Astrophysique et Planétologie, Observatoire Midi-Pyrénées, 14 avenue Édouard Belin, 31400 Toulouse, France

[3] Department of Earth Sciences, Carleton University, 1125 Colonel By Drive, Ottawa, ON, K1S 5B6, Canada (*correspondence: danielpeters@cunet.carleton.ca)

[4] Freie Universität Berlin, Institute of Geological Sciences, Malteserstrasse 74-100, 12249 Berlin, Germany

[5] University of Genova, Dipartimento di Scienze della Terra, Ambiente e Vita, Corso Europa 26, 16132 Genova, Italy

Abstract

The Erro Tobbio olivine-antigorite serpentinites and associated dehydration veins represent hydrated oceanic mantle rocks that escaped complete dehydration and recycling into the mantle after subduction to ~ 550-600 °C and 2.0-2.5 GPa. These rocks thus offer valuable insights into the petrological evolution of a slice of hydrated oceanic mantle and the geochemical cycling down to intermediate subduction zone depths. Our study emphasises the

role of brucite upon rock-buffered hydration and subduction dehydration employing bulk and *in situ* chemical data sets combined with petrology.

Bulk rock data reveal a coherent mantle peridotite slice affected by variable melt depletion and refertilisation. Subsequent fluid-rock interaction stages proceeded isochemically with respect to SiO_2, i.e., without significant SiO_2 enrichment characteristic for hydrothermal ocean floor serpentinisation. Relicts of low-*T* mesh textures after olivine and preservation of precursor mineral and low-*T* hydration geochemical features indicate a lack of subsequent fluid and metamorphic overprinting, even at scales of tens of micrometres. Fluid-mobile element enrichments are modest with exceptions for B and W. Enrichment signatures of U/Cs << 1 and Rb/Cs of 4-26 are characteristic of shallow forearc hydration within or atop the slab by fluids derived from breakdown of clays or first dehydration of altered oceanic crust with a subordinate sedimentary pore fluid component. Overall, the geochemical and petrological changes of the Erro Tobbio peridotites during fluid-rock interactions were rock-buffered, in contrast to fluid-buffered hydration accompanied with significant SiO_2 metasomatism at, e.g., mid ocean ridges.

Silica-neutral rock-buffered serpentinisation resulted in prominent brucite formation upon olivine hydration. In absence of excess SiO_2, subsequent serpentine transformation of chrysotile/lizardite to antigorite likely produced even more brucite. Rock-buffered fluid-rock interactions thus provide a mechanism for stabilising brucite in subduction zone serpentinites, presumably along hydration fronts and within deeper sections of the oceanic lithospheric mantle. Finally, brucite + antigorite dehydration produced up to 40 vol. % of metamorphic olivine and prominent olivine + Ti-clinohumite + magnetite vein networks at temperatures < 550-600 °C, prior to complete antigorite breakdown. Wall rocks released alkali elements, B, Cr, As, Sb, and Ba into the dehydration fluids, along with substantial Sr, REE and HFSE redistribution into vein minerals.

1. Introduction

Subduction zones are sites of major geological activity including hazardous seismicity, volcanism and large-scale element cycling between exogenous and endogenous reservoirs. Progressive dehydration of hydrated oceanic lithosphere during subduction releases large amounts of fluid-mobile element (FME)-rich fluids (e.g., Becker et al., 1999; John et al., 2004; Kessel et al., 2005; Spandler and Pirard 2013; Scambelluri et al., 2014) that can metasomatise the overlying mantle wedge (Bostock et al., 2002; Guillot et al, 2001; Zack and John, 2007; Deschamps et al., 2010) and play a crucial role in feeding arc magmatism (Brown et al., 1982; Hattori and Guillot, 2003; Marschall and Schumacher, 2012; Bali et al., 2012; John et al., 2012; Scambelluri and Tonarini, 2012). Moreover, dehydration reactions and escaping fluids are suspected to be linked to certain types of subduction zone seismicity (Hacker et al., 2003; Incel et al., 2017; Bloch et al., 2018; Taetz et al. 2018).

Serpentinites are thereby major water and fluid-mobile element carriers, containing up to 13 wt. % of structurally-bound H_2O combined with FME enrichments of up to 10^5 times primitive mantle concentrations (Hyndman and Peacock, 2003; Hattori and Guillot, 2007; Vils et al., 2008; Kodolányi et al., 2012). The stabilities of serpentine (Ulmer and Trommsdorff, 1995, Wunder and Schreyer, 1997) and chlorite (Fumagalli and Poli, 2004) from the ocean floor to subarc levels and beyond facilitate the preservation of chemical and structural records from fluid infiltration (Cannaò et al., 2015; 2016) and *in situ* dehydration fluid production (Plümper et al., 2017; Bloch et al., 2018) during subduction, and enable the transport of large amounts water and FMEs to arc source regions (e.g., Scambelluri and Philippot, 2001; John et al., 2004; Hattori and Guillot, 2003; Spandler and Pirard, 2013; Chen et al., 2019). Investigations of geochemical signatures recorded in serpentinites subducted to different depths hence allow for constraining dehydration-related element loss (Scambelluri et al. 2004; John et al., 2011; Kendrick et al., 2011, 2013; Lafay et al., 2013) and revealing potential interactions with externally derived fluids during subduction (Deschamps et al., 2010; Scambelluri et al., 2014;

74 Cannaò et al., 2015; 2016; Schwarzenbach et al., 2018). Together with structural and textural
75 relations in the field these geochemical data enable obtaining a detailed image of a fossil plate
76 interface, including its physical properties (Hermann et al., 2000; Angiboust et al., 2011; 2015;
77 Agard et el., 2016), and fluid transport mechanisms (John et al., 2012; Plümper et al., 2017;
78 Bloch et al. 2018; Taetz et al., 2018; Chen et al., 2019).

79 A variably important dehydration reaction in serpentinites at intermediate subduction zone
80 depths is the olivine-forming brucite + antigorite consumption at 400-550 °C (Padrón-Navarta
81 et al., 2013; Plümper et al., 2017; Bloch et al., 2018; Bretscher et al., 2018; Kempf and
82 Hermann, 2018), expelling up to a few wt. % of structurally-bound water and thus also fluid-
83 mobile elements (FMEs) into dehydration pathways (Scambelluri et al., 2001; De Hoog et al.,
84 2014; Cannaò et al., 2016; Plümper et al., 2017; Bloch et al., 2018; Gilio et al., 2019). Effective
85 loss into fluids or retention in the host serpentinites is not well-constrained for many FMEs,
86 however. Extensive formation of metamorphic olivine by this reaction further requires large
87 modes of brucite in subducting serpentinites, which would be produced following SiO_2-neutral
88 ("isochemical") serpentinisation (Malvoisin, 2015; Schwarzenbach et al., 2016). Present-day
89 ocean floor serpentinites are characterised by scarcity of brucite due to SiO_2 metasomatism
90 prevailing in fluid-dominated serpentinisation environments; i.e., when serpentinisation is non-
91 isochemical with respect to SiO_2 (Paulick et al., 2006; Boschi et al., 2008; Harvey et al., 2014;
92 Malvoisin, 2015).

93 The Erro Tobbio (Ligurian Alps, Italy) unit represent variably serpentinized oceanic mantle
94 rocks subducted to ~ 550-600 °C and 2.0-2.5 GPa (~ 70 km depth; Scambelluri et al., 1991;
95 1995; 1997). Cross-cut by olivine + Ti-clinohumite + magnetite dehydration veins linked to
96 brucite + antigorite consumption (Scambelluri et al., 1995, Plümper et al. 2017). The antigorite
97 serpentinites within this unit thus offer a unique opportunity to study fluid-mediated element
98 cycling from serpentinisation to partial dehydration at intermediate subduction zones depth
99 (Früh-Green et al., 2001; John et al., 2011; Scambelluri and Tonarini, 2012). We present a

100 detailed study of a suite of Erro Tobbio antigorite serpentinites addressing the role of brucite
101 and of SiO_2 metasomatism during hydration and subduction dehydration employing bulk and
102 *in situ* chemical data sets. Major to trace element signatures are used to constrain fluid
103 imprints, to derive implications on serpentinisation environments, and to reconstruct the
104 petrological evolution. Ultimately, vein and wall rock geochemistry are used to qualitatively
105 estimate the compositions of dehydration-related fluids.

106

107 2. Geological setting and sampling

108 The Erro Tobbio ultramafic unit is part of the Voltri Group in the Ligurian Alps (Fig. 1), which
109 represents remnants of the Jurassic Ligurian ocean and the suture zone between the
110 European and Adriatic plates after Alpine subduction. The (meta-)peridotites record partial
111 melting processes within the convecting asthenospheric mantle, followed by decoupling and
112 accretion to the overlying lithosphere with recrystallisation under spinel facies conditions
113 (Piccardo and Vissers, 2007). The subsequent lithospheric mantle stage was characterised
114 by a complex tectono-magmatic history in response to the formation of an ocean continent
115 transition zone induced by crustal thinning in an asymmetric oceanic rift (Hoogerduijn Strating
116 et al., 1993), associated uplifting and decompression of the spinel lherzolites starting in the
117 Permian (Rampone et al., 2004), and final opening of the slow spreading Ligurian Tethys in
118 the Late Jurassic. Development of km-scale shear zones during extensional deformation was
119 followed by multiple interactions with ascending MORB-type melts, i.e., local chemical
120 modification of the peridotites (i.e., melt-rock interactions and melt impregnation), and
121 recrystallisation under plagioclase-facies conditions (Fig. 1; Borghini et al., 2007; Piccardo and
122 Vissers, 2007).

123 Exposure to fluids at the Tethys ocean floor and/or during early subduction was accompanied
124 by variable serpentinisation of the peridotites (up to 15-100 %) at low temperatures (< 300 °C;

Scambelluri et al., 1991; 1995; 1997). Subsequent subduction was characterised by localised deformation and recrystallisation in the high-strain serpentinites (Hermann et al., 2000), and progressive dehydration up to 550-600 °C and 2.0-2.5 GPa induced serpentine mineral transformation to antigorite, formation of metamorphic olivine during brucite consumption, and growth of Ti-clinohumite and metamorphic diopside. Fluids released by the brucite-consuming reaction were effectively channelised into veins that crystallised the same metamorphic assemblage as in the wall rock serpentinites (Scambelluri et al. 1995; Plümper et al., 2017).

Several geochemical studies investigated the isotope ratio and trace element imprints acquired during serpentinisation in order to constrain the serpentinisation environment(s) of the Erro Tobbio serpentinites, and explored vein chemical signatures to constrain element release during subduction dehydration. Hydrogen and O (Früh-Green et al., 2001), and B (Scambelluri and Tonarini, 2012) isotope studies reported chemical differences between deformed and undeformed serpentinites, and assigned differences to localised and variable fluid imprints acquired at the ocean floor and during shallow subduction in a suprasubduction position. Halogen (John et al., 2011), noble gas (Kendrick et al., 2011, 2013) and N isotope (Halama et al., 2014) studies reported the influence of sedimentary/organic pore fluids during single-stage hydration, inferring a shallow depth of serpentinisation along faults in the bending slabs or within a suprasubduction environment by slab fluids. Cross-cutting veins have been shown to have crystallised from internally-derived fluids based on several isotope studies (Früh-Green et al., 2001; Bonifacie et al., 2008; Halama et al., 2014); however, only very limited trace chemical signatures of the veins have been presented in support of an internal origin of veining fluids derived from the brucite-consuming reaction (e.g., Scambelluri et al., 2001; John et al., 2011; Scambelluri and Tonarini, 2012). Furthermore, Philippot et al. (2007) proposed the ingress of an external mafic fluid component in the veins based on N and O isotope ratio systematics.

Antigorite serpentinites and dehydration vein samples investigated in this study were obtained during different sampling campaigns, with most of the samples having been employed and characterised in previous geochemical studies (ETCL samples series; John et al., 2011, Halama et al., 2014). Low- and high-strain antigorite serpentinites and associated veins were solemnly selected based on petrological and textural criteria, i.e., only rocks with a notable metamorphic olivine-bearing assemblage and minimal retrograde overprint were collected to cover deformed (high-strain) and undeformed (low-strain) structural subdomains in outcrops along the Gorzente river (Fig.1). Wall rock serpentinites were sampled along traverses perpendicular to the cross-cutting dehydration veins with 1.5-2.0 cm distance in-between the sub-samples to investigate potential geochemical profiles from the wall rocks into the veins or *vice versa*.

3. Analytical methods

3.1. Bulk rock analysis

Samples were analysed for bulk major and trace elements by LA-ICP-MS measurement of nanoparticulate pressed powder pellets (PPP) following the analytical protocol presented in Peters and Pettke (2017) and Garbe-Schönberg and Müller (2014). Measurements were conducted using a GeoLas-Pro 193 nm ArF Excimer laser system (Lambda Physik, Göttingen, Germany) connected to an ELAN DRC-e quadrupole mass spectrometer (Perkin Elmer, Waltham, MA, USA) at the University of Bern, Switzerland. Instrument optimisation ensuring robust plasma conditions closely followed procedures documented previously (Pettke et al., 2012; Peters and Pettke, 2017). External standardisation employed basalt glass GSD-1G from the United States Geological Survey (USGS). Data reduction used the program SILLS (Guillong et al., 2008) with robust limit of detection (LOD) calculation as presented in Pettke et al. (2012). Data reported per sample represent the mean with its 1 standard deviation

175 reproducibility of 6 spot measurements employing a 120 µm beam. The certified reference
176 material powders MUH-1 (serpentinised peridotite) and OKUM (komatiite) of the International
177 Association of Geoanalysts were analysed as unknowns together with the samples to monitor
178 the measurement trueness and reproducibility. The sample and standard measurement data
179 and day-specific optimisation parameters are documented in supplementary material Tab. 1.
180 For samples analysed previously with XRF and solution ICP-MS (see below) the existing bulk
181 rock powders were employed here for the production of PPP for LA-ICP-MS measurements.

182 Bulk rock major element concentrations for some sample powders were measured with a
183 Philips PW1480 X-ray fluorescence spectrometer, and trace element analyses by solution
184 ICP-MS were carried out with an Agilent 7500cs ICP-MS operating under standard conditions,
185 both at the Institute of Geosciences, Kiel University (Germany). The protocol used for sample
186 processing for solution ICP-MS analysis is detailed in Garbe-Schönberg (1993) and John et
187 al. (2008). Analytical results are averages of three replicate measurements after blank
188 subtraction, and measurement trueness and reproducibility were monitored analysing the
189 standard reference powders BHVO-2 (basalt, USGS) and UB-N (serpentinite, Association
190 Nationale de la Recherche Technique) as unknowns (supplementary material Tab. 1). The
191 loss on ignition (LOI) was determined by drying the samples at 120 °C in a drying cabinet for
192 24 h prior to heating in a ceramic oven to 1050 °C for 2 hours.

193 **3.2. Mineral chemical analysis**

194 Major element electron probe microanalysis (EPMA) of the rock-forming silicates were
195 performed on polished and carbon-coated thin sections using a JEOL JXA-8200 Superprobe
196 equipped with five wavelength dispersive X-ray spectrometers at the Institute of Geological
197 Sciences, University of Bern (Switzerland). All measurements were carried out with an
198 acceleration voltage of 15 kV, a beam current of 20 nA and a beam size of 5 µm as
199 compromise for simultaneous measurement of hydrous and anhydrous phases. Synthetic and
200 natural standards used for calibration were wollastonite (SiO_2, CaO), almandine (FeO),

forsterite (MgO), anorthite (Al_2O_3), albite (Na_2O), ilmenite (TiO_2), bunsenite (NiO), tephroite (MnO), scapolite (Cl), and phlogopite (F). Matrix effects were corrected for by employing the CITZAF algorithm (Armstrong, 1995). All EPMA data are reported in supplementary material Tab. 2.

In-situ major to trace element concentration measurements by LA-ICP-MS were carried out at the Institute of Geological Sciences, University of Bern (Switzerland) using the same system as for PPPs. Spot sizes were 60 µm for the external calibrator and ranged from 44 to 120 µm for in-situ measurements of single grains (olivine, Ti-clinohumite, diopside) and monomineralic clusters (antigorite, chlorite). Measurements of monomineralic clusters were only considered when the transient signal did not show any evidence of other phases, or integration intervals were set accordingly to avoid inclusions or interspersed other phases. The basalt glass GSD-1G was employed as matrix-close external calibrator for the mineral measurements, and the standard glass SRM 612 of the National Institute of Standards and Technology was measured as unknown to monitor the measurement trueness and reproducibility. Instrumental optimization strategies and data reduction procedures were identical to those reported above for PPP-LA-ICP-MS. Day-specific optimisation parameters and all LA-ICP-MS mineral and standard measurement data are listed in supplementary material Tab. 3. All LA-ICP-MS data were reduced employing SILLS and using total major element oxides for internal standardisation (e.g., Leach and Hieftje, 2000; Halter et al., 2002).

4. Results

4.1. Petrography

The Erro Tobbio massif encompasses massive (low-strain), variably serpentinised peridotites and serpentinites, locally cut by mylonitic (high-strain) antigorite serpentinite shear zones (Fig. 1). Along with metagabbros and metabasalts, this unit represents a classical example of subduction-metamorphosed slow-spreading oceanic lithosphere. The petrography of the

antigorite serpentinites and associated veins will now be described in detail for the high- and low-strain structural domains.

The high-strain antigorite serpentinites ETCL4-1b, ETCL4B1 and ETCL4B2 consist of a strongly foliated and fine-grained antigorite ± chlorite matrix with dispersed fine-grained olivine, magnetite, Ti-clinohumite, and diopside. The matrix embeds mm- to cm-sized porphyroclasts of relict mantle clinopyroxene exhibiting characteristic cleavage and hydrated exsolution lamellae (former orthopyroxene; Fig. 2a), along with pseudomorphs after completely serpentinised orthopyroxene and spinel. Olivine is exclusively metamorphic (see below) and occurs occasionally as large grains (Fig. 2b); however, most olivine is small and dispersed in the sheared matrix. The foliation is locally cross-cut by pure antigorite veinlets and olivine shear bands, with the latter overgrowing the former. Relict mantle clinopyroxene is variably serpentinised at the rims and along the exsolution lamellae with replacive antigorite, chlorite, diopside, Ti-clinohumite, and occasional magnetite. Spinel was pseudomorphically replaced by magnetite (in the core) and chlorite (corona around magnetite). Chlorite coronae thereby exhibit an optical zonation in crossed polarised light. Sulphides (undifferentiated) are common accessory phases in the matrix. Modal abundances of the rock-forming minerals are estimated to be ~ 70-75 % antigorite, 15-20 % olivine, 5-7 % chlorite, 3-5 % relict and metamorphic diopside, 1-2 % magnetite, and < 1 % Ti-clinohumite and sulphides.

Low-strain antigorite serpentinites are represented by samples ETCL7-1b, ETCL7-4, ETCL7-6, ETCL8-4 and ET08-16. In sample ET08-16 elongated and oriented relict mantle clinopyroxene and pseudomorphs after orthopyroxene and spinel preserve a pre-subduction mantle deformation texture (*cf* also Fig. 2a). The statically grown metamorphic assemblages of these samples consist of olivine + antigorite + diopside + chlorite+ Ti-clinohumite + magnetite, and different textural domains are developed. Static intergrowths of mm-sized metamorphic olivine along with µm to mm-sized antigorite blades are most common. Larger olivine can preserve relict mantle cores that are surrounded by relict mesh textures acquired

252 likely during low-temperature serpentinisation, which in turn were replaced by sub- to euhedral
253 antigorite blades or overgrown by metamorphic olivine (Fig. 3a). Millimetre- to cm-sized mantle
254 clinopyroxene is often preserved in the low-strain domains and variably pseudomorphically
255 serpentinised at the rims and along former orthopyroxene exsolutions with antigorite, chlorite,
256 diopside, Ti-clinohumite, and occasional magnetite (Fig. 3b). Locally, the metamorphic
257 assemblage in these bastite domains is complemented by minor proportions of olivine.
258 Metamorphic olivine and Ti-clinohumite contain numerous opaque and transparent inclusions
259 < 15 µm, dominantly magnetite and antigorite. Pseudomorphs after completely serpentinised
260 orthopyroxene are characterised by small interspersed grains of metamorphic diopside and
261 olivine embedded in the replacive antigorite (Fig. 3c).

262 Patches of almost pure anhedral and unoriented antigorite with only minor magnetite and
263 metamorphic olivine are dispersed throughout the samples and are often found between
264 abundant cm-sized domains of static olivine + antigorite intergrowths. Spinel is completely
265 replaced by pseudomorphic magnetite and chlorite (Fig. 2d), where magnetite forms the core
266 and chlorite the rims of the pseudomorphic assemblage. Modal abundances of the phases in
267 the low-strain antigorite serpentinites vary between 45-65 % for antigorite, 25-40 % for olivine
268 (the sum of relict and metamorphic olivine), 5-10 % for relict mantle clinopyroxene and
269 metamorphic diopside, 2-5 % for chlorite, 2-3 % for Ti-clinohumite, 1-2 % for magnetite, and
270 < 1% for minor sulphides.

271 The metamorphic assemblage of the antigorite serpentinites is cross-cut by veins containing
272 variable modes of cm-sized olivine, Ti-clinohumite, and magnetite with subordinate amounts
273 of diopside, chlorite and antigorite (Fig. 2c,d; 3e,f). Colourless vein olivine sometimes exhibits
274 brighter patches in BSE images and, locally, yellow olivine is abundant, even in contact with
275 colourless olivine and Ti-clinohumite. Ti-clinohumite further appears to overgrow olivine (Fig.
276 2c). Vein olivine and Ti-clinohumite crystals contain many < 15 µm sized inclusions of
277 transparent and opaque phases as well as rare multiphase fluid inclusion relicts. Diopside is

mostly present in fine-grained domains crystallised along shear bands cutting through the veins in high-strain serpentinites (Fig. 2d), along fractures in olivine together with chlorite, or as prismatic to needle-shaped crystals that curve around or pierce into vein olivine and Ti-clinohumite (Fig. 3e,f). Olivine fragments enclosed within diopside + chlorite assemblages are often completely serpentinised (Fig. 3f). Diopside crystals contain a high number of solid (transparent and opaque), and primary and secondary multiphase fluid inclusions. Olivine is usually serpentinised along cracks with a very fine-grained, greenish mixture along cracks. It is hence emphasised that all vein samples record variably prominent retrogression as is also evident from high LOI values (see data below, and LOI values of up to 11.3 wt. % for vein samples in Scambelluri et al., 2001).

4.2. Bulk rock chemistry

Bulk rock data presentation is summarised into antigorite serpentinite and vein data, with differences between the low- and high-strain domains being addressed in the discussion. The entire dataset is tabulated in the supplementary material Tab. 1.

Antigorite serpentinites

The Erro Tobbio metaserpentinites are variably melt-depleted, refertilised, and hydrated mantle rocks that record different extents metamorphic overprint. Metaperidotite compositions are lherzolitic to harzburgitic and follow the trends of residual mantle rocks after melt extraction (Fig. 4a). This is also reflected by the range in X_{Mg} (molar Mg/(Mg+Fe); all Fe considered to be Fe^{2+}) of between 0.89 and 0.93 that corresponds to typical mantle rocks, and by variably lowered concentrations of Al_2O_3 and CaO that range from 1.19 to 2.88 wt. % and 0.22 to 3.61 wt. % (Fig. 4b), respectively. Water contents (displayed as LOI because carbonates are negligible in our samples) are higher in the high-strain antigorite serpentinites with = 11.2-12.3 wt. %, while the low-strain domains are less hydrated with = 7.6-10.0 wt. %.

303 Transition metal concentration ranges are 7.5-15.6 µg g^{-1} for Sc, 35-80 µg g^{-1} for V, 1540-3730
304 µg g^{-1} for Cr, 78-116 µg g^{-1} for Co, and 1180-2120 µg g^{-1} for Ni. The rare earth elements
305 (REEs), which are thought not to be significantly mobile during serpentinisation (e.g., Allen
306 and Seyfried, 2005) show primitive mantle (PM) normalised patterns (Fig. 4c) strongly
307 depleted in light REEs (La = 0.01-0.04 x PM) and moderately depleted in middle and heavy
308 REEs (Gd = 0.1-0.06 x PM; Lu = 0.3-0.6 x PM), without a Eu anomaly as is often observed for
309 abyssal serpentinites (e.g., Niu, 2004) and subducted equivalents. Serpentinites from low-
310 strain domains exhibit larger trace element variability than those from high-strain domains.

311 In a PM-normalized trace element distribution diagram (Fig. 5a), the high-field strength
312 elements are variably depleted without domain-related differences; hence, they record
313 variable melt depletion in analogy to major element systematics. To the contrary, typical fluid
314 mobile elements are variably enriched (Fig. 5a), most prominently so for B and W with up to
315 100 x PM. Moderate enrichments are observed in Cs, Bi, Pb, As, Sb, and Mo of up to 10 x PM
316 (Fig. 5a). Rubidium, Ba, U, Sr, K, Be, Li, and the chalcophile elements Tl, Cd, In, and Sn
317 appear variably enriched relative to the indicated melt depletion trend (Fig. 5a).

318 *High-pressure veins*

319 Major element compositions of the H*P* dehydration veins are highly variable due varying modal
320 abundances of the coarse-grained vein-forming minerals. In particular, compositional ranges
321 for SiO_2 = 34.3-41.3 wt. %, X_{Mg} = 0.80-0.87, and CaO = 0.3-5.88 wt. % are prominently larger
322 than in the wall rock serpentinites. Variable contents of $Al_2O_3 \leq 1.04$ wt. % and TiO_2 = 0.09-
323 0.52 wt. % are accompanied by narrow MnO ranges of = 0.18-0.23 wt. %. The veins further
324 display elevated P_2O_5 concentrations of up to 0.23 wt. %, and water contents vary between
325 4.8 and 8.3 wt. % LOI. One strongly retrogressed vein contains 12.1 wt. %.

326 In a PM-normalised trace element distribution diagram (see Fig. 5b) the patterns of vein bulk
327 samples largely mirror those of the host serpentinites, without systematic differences between

high-strain and low-strain domains. Yttrium and REE concentrations vary over one order of magnitude with, e.g., Gd = 0.2-0.8 x PM and Tm = 0.2-1 x PM. REE patterns are similar to those of the wall rocks with LREE depletion relative to MREEs and HREEs but exhibit minor enrichments in Yb and Lu (up to 1.5 x PM; Fig. 5b). One vein (ETCL4B2-VEIN) displays distinctly higher LREE abundances (e.g., La = 0.1 x PM; Fig. 5b). High field strength element abundances are similar (Zr = 0.78-1.2 μg g^{-1}, Hf = 0.032-0.058 μg g^{-1}) or enriched relative to wall rocks (Nb = 0.018-0.068 μg g^{-1}; Ta = 0.001-0.003 μg g^{-1}; Fig. 5b). Transition metals are abundant at Sc = 15-48 μg g^{-1}, V = 30-48 μg g^{-1}, Cr = 697-1110 μg g^{-1}, Co = 122-170 μg g^{-1}, Ni = 1610-2280 μg g^{-1}, and Zn = 46-63 μg g^{-1}.

Alkali and alkaline earth metals concentrations range for Li = 1.9-5.1 μg g^{-1}, Rb = 0.022-0.07 μg g^{-1}, Sr = 4.1-30 μg g^{-1}, Cs = 0.011-0.029 μg g^{-1}, and Ba = 1.9-6.2 μg g^{-1}. Three data points for B reveal enrichments of up to 22 μg g^{-1}, and U and Th concentrations are below LOD except for one sample. Concentrations of chalcophile elements in the veins are at wall rock levels or slightly elevated with As $\leq$ 0.059 μg g^{-1}, Sb $\leq$ 0.027 μg g^{-1}, Pb = 0.27-0.55 μg g^{-1}, and Bi contents of up to 0.01 μg g^{-1}. Abundances of the siderophile elements Mo and W range from 0.116-0.294 μg g^{-1} and 0.051-0.33 μg g^{-1}, respectively.

4.3. Mineral chemistry

Mineral data are presented by addressing each mineral separately, and major element data represent combined EPMA and LA-ICP-MS data since both are in very good agreement. Chemical compositions are only briefly summarised here for key elements, while details, e.g., texture-related differences, will be presented more thoroughly in the discussion when required. The entire data set is tabulated in supplementary materials Tab. 2 (EPMA data) and Tab. 3 (LA-ICP-MS data).

Olivine

Olivine in the Erro Tobbio antigorite serpentinites and dehydration veins is variably forsteritic with X_{Mg} between 0.77 and 0.90. TiO_2 concentrations are generally ≤ 0.1 wt. % with exceptions of some yellowish olivine grains containing up to 0.82 wt. % TiO_2. MnO and NiO concentrations range from 0.013 to 1.26 wt. % and 0.12 to 0.45 wt. %, respectively, while Cr is below 100 µg g^{-1}. Alumina, CaO, and Na_2O concentrations are generally very low; few grain cores contain up to 0.027 wt. % of Al_2O_3 and up to 0.092 wt. % of CaO, and 0.034 wt.% of Na_2O, however.

REE patterns display a strong depletion in LREEs (Ce = 0.001-0.005 x PM) relative to HREE (Lu = 0.04-5 x PM). Lithium and Sc are abundant at lower concentrations in matrix olivine (Li ≤ 8.0 µg g^{-1}; Sc ≤ 43 µg g^{-1}) than in vein olivine, where these elements are variably enriched (Li up to = 19 µg g^{-1}; Sc up to = 83 µg g^{-1}). Boron concentrations are mostly ≤ 5 µg g^{-1} but rise to = 54 µg g^{-1} in some olivine grains.

Antigorite

Antigorite in veins and wall rocks is Mg-rich with tightly clustering X_{Mg} of between 0.94 and 0.97. Alumina and Cr_2O_3 concentrations vary up to 3.49 wt. % and 1.04 wt. %, respectively. Manganese concentrations in all but one antigorite grain are below 0.07 wt. % MnO, and NiO abundances are ≤ 0.25 wt. % with a tendency towards higher NiO in low-strain domain antigorite. Concentrations of TiO_2 ≤ 0.03 wt. %, CaO ≤ 0.1 wt. %, and Na_2O ≤ 0.06 wt. % are generally low in all analysed grains. Chlorine in matrix and vein antigorite of high-strain domains is low (≤ 0.03 wt. %) while concentrations of up to 0.15 wt. % were measured in matrix and vein antigorite of low-strain domains.

Rare earth element patterns and Y (not shown) are depleted towards LREE (e.g., La = 0.001-0.02 PM vs. Lu = 0.03-0.2 PM), and concentration ranges for the different structural domains are mostly overlapping. Transition metal contents are highly variable for V = 8-140 µg g^{-1}, Cr = 29-6700 µg g^{-1}, and Ni = 85-1380 µg g^{-1}, while distributions are more homogeneous for Sc = 3-12 µg g^{-1}, Co = 24-62 µg g^{-1}, and Zn = 25-42 µg g^{-1}. High-field strength element

abundances in antigorite overlap between the structural domains with Zr = 0.074-1.5 μg g^{-1}, Nb = 0.005-0.028 μg g^{-1} and Hf ≤ 0.085 μg g^{-1}. Tungsten concentrations are usually ≤ 0.02 μg g^{-1} but occasionally are as high as 0.12 μg g^{-1}.

Boron concentrations scatter non-systematically between domains and textural context from 4.2 μg g^{-1} to 30 μg g^{-1}. Alkali and alkaline earth metal abundances are low with Li < 0.045 μg g^{-1}, Sr = 0.04-1.4 μg g^{-1}, Cs ≤ 0.034 μg g^{-1}, and Ba ≤ 0.61 μg g^{-1} in low-strain domains, and tend to be higher in higher in the high-strain serpentinites: Li ≤ 0.27 μg g^{-1}, Rb ≤ 0.52 μg g^{-1}, Sr = 0.16-1.3 μg g^{-1}, Cs ≤ 0.40 μg g^{-1}, and Ba ≤ 3.7 μg g^{-1}. Arsenic concentrations in antigorite are mostly below 0.06 μg g^{-1} but 0.13 μg g^{-1} in low-strain domains and 0.03 μg g^{-1} in high-strain domains independent of textural context. Few significant measurements yielded Sb ≤ 0.02 μg g^{-1}. Antigorite from cross-cutting antigorite veinlets has intermediate compositions for all trace elements, and no trace element data could be obtained for antigorite in the dehydration veins (due to the small crystal size and frequent inclusions).

Ti-Clinohumite

Titania concentrations in matrix and vein Ti-clinohumite vary between 3.25 and 5.19 wt. % with X_{Mg} = 0.84-0.90. Minor constituents are MnO = 0.26-0.53 wt. %, NiO ≤ 0.31 wt. %, and Cr_2O_3 ≤ 0.10 wt. %. Alumina (≤ 0.038 wt. %) and CaO (≤ 0.044 wt. %), Na_2O (≤ 0.05 wt. %), and Cl (≤ 0.1 wt. %) abundances are low in all analysed grains except for two outliers with high Na_2O (0.40 and 0.52 wt. %) and Cl (0.30 and 0.93 wt. %), for which we suspect the influence of (submicroscopic) fluid inclusions.

The high field strengths elements are variably enriched with Zr = 1.5-15 μg g^{-1}, Nb = 0.012-0.68 μg g^{-1}, Hf = 0.032-0.51 μg g^{-1}, Ta = 0.002-0.022 μg g^{-1}, and W = 0.014-0.45 μg g^{-1}. Rare earth element patterns (not shown) are only available for MREE to HREE (Dy-Lu) and display strong depletion towards lighter REEs (Lu = 1-3 x PM to Dy = 0.009-0.03 x PM). Transition metal abundances range from 126 to 187 μg g^{-1} for Co, 1050-2500 μg g^{-1} for Ni, and Sc and

Zn concentrations are as high as 57 μg g^{-1} and 119 μg g^{-1}, respectively. Boron concentrations in Ti-clinohumite from veins and wall rocks range from 5 to 37 μg g^{-1}. Other notable element abundances are Li ≤ 12 μg g^{-1}, Rb ≤ 0.028 μg g^{-1}, Sr ≤ 1.4 μg g^{-1}, and Ba ≤ 2.9 μg g^{-1}.

Diopside

Clinopyroxene in the Erro Tobbio serpentinites and dehydration veins is diopsidic. Relict mantle clinopyroxene displays X_{Mg} = 0.90-0.93 with 20.9-23.6 wt. % of CaO, while metamorphic and vein diopside contains CaO = 24.5-27.6 wt. % with X_{Mg} ranging from 0.94 to 0.98. Mantle clinopyroxene is characterised by TiO_2 contents of up to 0.63 wt. %, Al_2O_3 = 4-7.43 wt. %, Cr_2O_3 = 0.59-1.22 wt. %, and Na_2O = 0.35-0.84 wt. % compared to TiO_2 ≤ 0.12 wt. %, Al_2O_3 ≤ 1 wt. %, Cr_2O_3 ≤ 0.3 wt. %, and Na_2O ≤ 0.35 wt. % in metamorphic and vein diopside.

Trace element data are limited to few relict mantle clinopyroxene and vein diopside measurements since small grain sizes and abundant inclusions did not allow for clean LA-ICP-MS analysis of metamorphic diopside in the wall rocks. Medium and heavy REEs and Y are abundant at 2-6 x PM in relict mantle clinopyroxene whereas measured concentrations for these elements in vein clinopyroxene scatter towards lower values (down to 0.3 x PM for Sm-Lu and Y). Light rare earth elements are increasingly depleted with decreasing atomic mass from Nd = 1 x PM to La = 0.04 x PM in both clinopyroxene types. Concentrations of HFSEs in relict clinopyroxene are high with Zr = 6-7 μg g^{-1}, Nb = 0.035-0.036 μg g^{-1}, and Hf = 0.35-0.40 μg g^{-1}, and lower in metamorphic vein diopside with Zr ≤ 0.75 μg g^{-1}, Nb ≤ 0.004 μg g^{-1}, and Hf ≤ 0.07 μg g^{-1}.

Vein diopside exhibits high and variable alkaline earth metal concentrations with Sr = 19-56 μg g^{-1} and Ba = 0.05-5.6 μg g^{-1} compared to Sr = 0.31-4.8 μg g^{-1} and Ba ≤ 0.17 μg g^{-1} in relict mantle clinopyroxene. Lithium abundances are 5.8-8.3 μg g^{-1} in relict clinopyroxene and 0.7-8.3 μg g^{-1} in vein diopside, which exhibits Rb enrichments of up to 0.067 μg g^{-1}. Boron and Pb

concentrations are low in relict clinopyroxene (B ≤ 0.37 µg g^{-1}; Pb ≤ 0.016 µg g^{-1}) but range from 4.7-9.3 µg g^{-1} and up to = 0.21 µg g^{-1} in vein diopside, respectively.

Chlorite

Chlorite is Mg- and Al-rich with X_{Mg} between 0.93 and 0.95, and Al_2O_3 = 11.4-18.2 wt. % in the matrix and Al_2O_3 = 7.15-11.3 wt. % in the veins. TiO_2 ≤ 0.022 wt. %, Cr_2O_3 ≤ 2.38 wt. %, MnO = 0.015-0.048 wt. %, NiO =0.049-0.24 wt. %, CaO ≤ 0.053 wt. %, and Cl concentrations ≤ 0.024 wt. % vary randomly. Sodium concentrations significantly differ between the strain domains, ranging from 0.073 wt. % to 0.138 wt. % in the high-strain domains, while Na_2O ≤ 0.045 wt. % in the low-strain domains.

The REE patterns in chlorite (not shown) display LREE depletion (Ce = 0.002-0.02 x PM) relative to MREEs (Sm = 0.01-0.08 x PM) and HREEs (Lu = 0.02-0.1 x PM). Transition metal abundances are V = 71-134 µg g^{-1}, Cr = 1750-11800 µg g^{-1}, Co = 34-64 µg g^{-1}, and Ni = 350-1560 µg g^{-1}. Most alkali and alkaline earth element concentrations are higher in matrix chlorite of high-strain domains for Li = 0.13-0.20 µg g^{-1}, Sr = 0.72-0.89 µg $g^{-1)}$, Cs = 0.003-0.053 µg g^{-1}, and Ba = 1.1-1.8 µg g^{-1} than in matrix chlorite of low-strain domains with Li ≤ 0.10 µg g^{-1} (one outlier at 0.23 µg g^{-1}), Sr = 0.092-0.74 µg g^{-1}, Cs = 0.003-0.053 µg g^{-1}, and Ba = 0.047-0.88 µg g^{-1}, while K ≤ 400 µg g^{-1} and Rb ≤ 1.3 µg g^{-1} in some matrix chlorites of low-strain domains are higher than in the high-strain serpentinites (K ≤ 22 µg g^{-1}, Rb ≤ 0.21 µg g^{-1}). Vein chlorite exhibits lower concentrations than matrix chlorite (Li = 0.062-0.18 µg g^{-1}; K = 1.3-16 µg g^{-1} with one outlier at 40 µg g^{-1}; Rb = 0.010-0.16 µg g^{-1}; Sr = 0.13-0.71 µg g^{-1} with one outlier at 3.8 µg g^{-1}; Cs = 0.004-0.12 µg g^{-1}; Ba = 0.12-1.2 µg g^{-1}). Boron abundances range from 1.6 to 9.8 µg g^{-1} in matrix and vein chlorite.

5. Discussion

5.1. Mantle protolith and initial compositional variability

Major and immobile trace element abundances in relict mantle minerals and bulk rock peridotite were usually considered to not change prominently during serpentinisation (e.g., Niu, 2004; Rampone et al., 2004; Kodolányi et al., 2012) and metamorphism (Deschamps et al., 2013), with location- and condition-specific exceptions of MgO loss by marine weathering (Snow and Dick, 1995), SiO_2 metasomatism (Bach et al., 2004; Paulick et al, 2006), or $CaCO_3$ addition during carbonation (Bideau et al., 1991). A recent study by Malvoisin (2015) revealed, however, that SiO_2 metasomatism, i.e., non-isochemical serpentinisation with respect to SiO_2, is very common in ocean floor serpentinites.

Erro Tobbio antigorite serpentinites plot tightly along the melt depletion trend in MgO/SiO_2 vs Al_2O_3/SiO_2 representation (the terrestrial array after Niu (2004) in Fig. 4a), indicating no significant MgO loss nor SiO_2 enrichment during the entire serpentinisation - subduction - exhumation cycle. The plot of Al_2O_3 vs. CaO (Fig. 4b) reveals some scatter around the melt depletion trend, with a few low-strain serpentinites showing enriched CaO for their respective Al_2O_3. Coupling of CaO with Al_2O_3 and REE systematics (Fig. 4b,d) identifies variable diopside modes as the cause for the correlation deviating from the melt depletion trend. Major element compositional variability solemnly related to partial melting or melt-rock interactions thus reveals that subsequent fluid-rock interactions were isochemical with respect to major elements. The chemical homogeneity within the Erro Tobbio unit (e.g., Fig. 4c, d) corroborates that it likely represents a coherent slice of hydrated and subducted oceanic mantle (e.g., Scambelluri et al., 1991; Rampone et al. 2004, 2005).

Mantle relict features also exist at mineral scale. Relict mesh textures after olivine in the low-strain antigorite serpentinites contain occasional darker cores in back-scattered electron (BSE) images that identify relict mantle olivine. It is characterised by X_{Mg} ~ 0.9 along with

475 elevated CaO, Al_2O_3, Na_2O, and the lowest MnO (~ 0.17 wt. %; Fig. 6a) and B concentrations
476 of all measured olivine crystals (Fig. 6b; < 0.3 µg g^{-1}; this study; Scambelluri et al., 2004) and
477 differs from the BSE-lighter metamorphic rims with lower X_{Mg} values. These olivine core
478 compositions correspond well to mantle olivine major element compositions reported for Erro
479 Tobbio (Fig. 6a; Scambelluri et al., 1991; Rampone et al. 2004, 2005). Non-serpentinised relict
480 mantle olivine in mesh centres together with antigorite overgrowing the low-*T* serpentine mesh
481 textures closely resembles textures documented for the chrysotile/lizardite to antigorite
482 transformation documented in a serpentinite from DSDP core Leg 84 Site 566 (Kodolányi and
483 Pettke, 2011; compare their Fig. 2d with Fig. 3a in this study).

484 Because compositional re-equilibration during the subduction cycle is subordinate notably for
485 the low strain domains, the two main hydrous phases antigorite and chlorite exhibit fluid-
486 immobile element compositional characteristics that can be ascribed to parent mineral
487 compositions (e.g., Deschamps et al., 2010; Kodolányi et al., 2012). Higher Sc, V and Cr (Fig.
488 6c), Y, Zr, and REE (Fig. 6d) concentrations in antigorite after pyroxene than in antigorite after
489 olivine in the low-strain domains indicate inheritance of these elements from precursor
490 pyroxene. Similar bimodal tendencies are observed for antigorite within the high-strain
491 antigorite serpentinites but overlap between the two compositional end members is common.
492 This overlap likely relates to re-equilibration during subduction metamorphism. Similar bimodal
493 compositions depending on the precursor mineral are indicated for chlorite in the low-strain
494 antigorite serpentinites. Chlorite after clinopyroxene thereby appears to contain higher
495 amounts of e.g., CaO, Na_2O, Sc, Y, and Zr, Hf, REEs, while chlorite after spinel exhibits higher
496 concentrations of Al_2O_3, Nb, and also Cr (not shown).

497

498 **5.2. Initial fluid-mobile element imprints**

499 Prominent enrichments of FMEs during hydration of mantle rocks are well-documented in
500 literature and can be used for constraining fluid origins and serpentinisation environments,
501 even for partially dehydrated serpentinites (Guillot et al., 2001; Kodolányi et al. 2012;
502 Deschamps et al., 2013; Peters et al., 2017). Compositional variability of bulk rock FME
503 contents in the antigorite serpentinites covers one order of magnitude (Fig. 5a; Tab. 1), and
504 primitive mantle-normalised trace element patterns are overall uniform for the different
505 structural domains. The strong B and W bulk rock enrichments (Fig. 5a) along with moderate
506 enrichments in Cs, Rb, Pb, As, and Sb readily identify hydration by a fluid of oceanic or
507 possibly early subduction origin (Guillot et al., 2001; Scambelluri et al., 2004; Kodolányi et al.,
508 2012; Deschamps et al., 2013; Andreani et al., 2014; Peters et al., 2017).

509 Fluid-mobile element patterns in antigorite and chlorite spanning over orders of magnitude
510 (Fig. 7,8) indicate disequilibrium, i.e., no or very poor re-equilibration during metamorphism,
511 at the µm- to mm-scale. Antigorite from high-strain domains generally incorporates < 200 µg
512 g^{-1} of Cl, which is consistent with bulk rock levels (141-210 µg g^{-1}; John et al., 2011) and
513 identifies antigorite as main Cl-carrier. In the low-strain domains, Cl concentrations in many
514 antigorite grains of up to ~ 900 µg g^{-1} are higher than respective bulk rock concentrations of
515 up to 254 µg g^{-1} and negatively coupled with X_{Mg} (Fig. 8a). In Guatemala forearc serpentinites,
516 Kodolányi and Pettke (2011) attributed the positive correlation between Cl and Fe abundances
517 with a concomitant lack of SiO_2 to the abundance of Fe-rich hydroxides such as iowaite that
518 can be submicroscopically intergrown with low-*T* serpentine phases. The apparent
519 preservation of this low-*T* serpentinisation feature supports limited resetting of the residual
520 hydrous phases and that associated characteristics should mainly represent *in situ* chemical
521 features obtained during respective hydration events.

522 Strontium concentrations are tendentially higher in antigorite and chlorite within high-strain
523 domains than within low-strain domains, and in antigorite after pyroxene compared to

antigorite after olivine within each structural domain. Precursor mineral concentrations are rarely exceeded. This indicates that most of the fluid-enriched Sr is stored in metamorphic diopside (and respective precursor hydration products), as is corroborated by coupling of Sr enrichments with CaO concentrations (Fig. 8b) at the bulk and mineral scale. Boron is evenly distributed between antigorite and chlorite and the respective textural domains (Fig. 7b, 8c). Magnitudes of B enrichment thereby largely balance the bulk rock budgets but require other B-rich phases, which appear to be metamorphic olivine (*cf* Scambelluri et al., 2004; De Hoog et al., 2014) and Ti-clinohumite (Fig. 7b, 8c). Neither Sr nor B mineral contents are thus suitable tracers of changing serpentinisation fluid compositions.

Rubidium, Cs and Ba are notably enriched relative to precursor mineral concentrations. Whereas Rb and Cs contents cover bulk rock compositional ranges, Ba concentrations are generally lower and require another Ba sink (Fig. 7d, e, f). Considering that clinopyroxene is the only Ca-phase in our rocks, we suspect metamorphic diopside to host the majority of Ba (see also vein diopside analyses; supplementary material 3). Enrichment ratios of Rb/Cs (Hulme et al., 2010; Kahl et al., 2015; Peters et al., 2017; Albers et al., in review) in antigorite and chlorite thus appear to represent the most promising tracer of undisturbed serpentinising fluid characteristics.

Indeed, Rb/Cs reveal two well-defined enrichment trends representing a main hydration fluid imprint with Rb/Cs of 0.5-4 in the majority of antigorite, chlorite, and the bulk rock data, and another minor component with Rb/Cs up to 24 in samples ETCL7-4 and ETCL8-4 (Fig. 8d). The bulk rock and most mineral Rb/Cs of sample ETCL7-4 fall along the main serpentinisation trend, indicating that high Rb/Cs mineral signatures are locally limited to few textural sites. Similarly, mineral data in sample suite ETCL8-4 plot along the main enrichment trend with exception of one chlorite analysis (Rb/Cs ~ 16), revealing the non-pervasive nature of the high Rb-Cs imprints. Rb/Cs > 10 in serpentine are unusual for forearc serpentinites (Peters et al., 2017; Albers et al., in review) and indicate either very shallow forearc pore fluids (Albers et al.,

550 in review) or even a minor ocean water component with Rb/Cs > 100 (Hulme et al., 2010;
551 Peters et al., 2017). The main dehydration fluid composition fingerprints breakdown fluids of
552 clay-rich sediment with or without first dehydration fluids from altered oceanic crust, rather
553 than (shallower) pore fluids (Kahl et al., 2015; Albers et al., in review). It thus appears likely
554 that the high Rb/Cs imprints represent first fluid ingresses along cracks and faults prior to the
555 main serpentinisation event at slightly deeper forearc levels. Hydration with forearc fluids is
556 corroborated by U/Cs < 1 in the same sample suite (Peters et al., 2017).

557 Based on the sensitivity of Rb/Cs to different fluid sources (Hulme et al., 2010; Kahl et al.,
558 2015; Peters, et al., 2017; Albers et al., in review) and the tightly-constrained main
559 serpentinisation trend, higher absolute enrichments in antigorite after pyroxene compared to
560 antigorite after olivine, and in high-strain serpentinites compared to low-strain serpentinites
561 can be attributed to variable fluid-mineral partitioning (based on higher initial alkali contents;
562 our preferred hypothesis), higher fluid-rock ratios or more concentrated fluids derived from the
563 same source.

564

565 **5.3. The relevance of brucite in precursor serpentinites**

566 Stable phases and reactions in serpentinites are highly dependent on the activity of SiO_2
567 throughout the serpentinisation-subduction-exhumation cycle (Bach et al., 2004: Frost and
568 Beard, 2007: Klein et al., 2009; Schwarzenbach et al., 2016). External SiO_2 input and
569 subordinate internal SiO_2 re-distribution during hydration of pyroxene (Toft et al., 1990) are
570 common, limiting stable brucite modes in ocean floor and forearc serpentinites (Bach et al.,
571 2004; Malvoisin, 2015). In the Erro Tobbio antigorite serpentinites, however, the olivine-
572 forming reaction

573 Antigorite + Brucite = 2 Olivine + 3 H_2O (1)

574 is considered to have been the main dehydration reaction (Scambelluri et al. 1995; Plümper
575 et al., 2017) during subduction to 550-600 °C and 2.0-2.5 GPa. With maximum concentrations
576 of MnO ~ 0.35 wt. % (Rampone et al. 2004; 2005) and B < 0.3 µg g^{-1} (this study; Scambelluri
577 et al., 2004) in pristine mantle olivine of Erro Tobbio (grey field in Fig. 6b; supplementary
578 material 3), it becomes evident that the vast majority of olivine (up to ~ 40 vol. %;
579 supplementary material 4) is non-mantellic with lower X_{Mg} and MnO, and notably enriched in
580 B (Fig. 6a,b). Sole diffusive olivine re-equilibration with surrounding phases during subduction
581 metamorphism thereby appears unlikely, as X_{Mg} zonations in olivine indicate disequilibrium at
582 the µm-scale (Fig. 3a). Frequent inclusions of magnetite or antigorite in olivine demonstrate
583 overgrowth, i.e., olivine formation by metamorphic reactions at the expense of former hydrous
584 phase(s) that were produced along with magnetite upon hydration. The rare occurrence of
585 mantle relicts (notably clinopyroxene) suggests that initial hydration was close to completion
586 even in the low-strain domains.

587 Following reaction (1), such high metamorphic olivine modes in the Erro Tobbio antigorite
588 serpentinites require substantial initial brucite modes, the likelihood of which is now
589 addressed. Silica-neutral rock-buffered serpentinisation of the peridotites (section 5.1) thereby
590 allows for reconstructing prograde reaction paths. In a SiO_2 preserving system, olivine
591 hydration proceeds via

592 $$2\ \text{Olivine} + 3\ H_2O = \text{Serpentine} + \text{Brucite} \quad (2)$$

593 and

594 $$\text{Olivine} + H_2O = \text{Serpentine} + \text{Magnetite} + \text{Brucite} + H_{2(aq)} \quad (3),$$

595 with reactions (2) and (3) being dependent on temperature, SiO_2 activity, fluid-rock ratios, and
596 the degree of serpentinisation (Frost and Beard, 2007; Andreani et al., 2013; Evans et al.,
597 2013; Klein et al., 2014)

598 Orthopyroxene is hydrated via (after Bach et al. 2006; Klein et al., 2009)

599 3 Orthopyroxene + 2 H_2O = 2 Serpentine + 2 $SiO_{2(aq)}$ (4).

600 Consumption of brucite by internally-derived SiO_2 released upon pyroxene hydration is then
601 possible via (Bach et al. 2006; Klein et al., 2009)

602 3 Brucite + 2 $SiO_{2(aq,\ opx)}$ = Serpentine + H_2O (5)

603 and

604 57 Brucite + 30 $SiO_{2(aq,\ opx)}$ = 15 Serpentine + 4 Magnetite + 23 H_2O + 4 $H_{2(aq)}$ (6).

605 Considering the harzburgitic compositions of the Erro Tobbio peridotites with 73-82 vol. % of
606 olivine and 11-17 vol. % of orthopyroxene (Rampone et al. 2004: chemical variability in
607 MgO/SiO_2 and Al_2O_3/SiO2 is comparable with our samples), i.e., molar olivine:orthopyroxene
608 ratios of up to 6:1 in the most primitive peridotites, silica released from pyroxene hydration can
609 only consume up to one third of all brucite produced during complete and SiO_2-neutral olivine
610 hydration (supplementary material 4; *cf* also Malvoisin, 2015). Note that chlorite formation after
611 spinel further reduces the amount of SiO_2 available from pyroxene hydration, and
612 clinopyroxene hydration is subordinate at best. Consequently, large brucite modes are
613 expected for rock-buffered serpentinisation environments.

614 Upon prograde metamorphism, chrysotile/lizardite will react to form antigorite in a SiO_2-
615 preserving system (Evans, 2004) via

616 Chrysotile/Lizardite = Antigorite + 3 Brucite (7).

617 The sluggish and highly *T*-dependent reaction (7) is thereby considered to be the main
618 serpentine phase transformation reaction in a SiO_2-preserving system (Evans 2004; Kodolányi
619 and Pettke, 2011; Evans et al. 2013), while other olivine-producing reactions are metastable

620 (Evans, 2004) and thus not considered here. Antigorite inclusions in olivine further require
621 antigorite stability prior to olivine formation.

622 In a third step, the major olivine-forming and H_2O-liberating reaction (1) proceeded leading to
623 the formation of the olivine-rich dehydration veins in equilibrium with the antigorite
624 serpentinites (after Evans, 2004; 2010; Plümper et al., 2016). Other major olivine-forming
625 reactions, which involve antigorite breakdown and talc or orthopyroxene formation, proceed
626 at temperatures above those reached by the Erro Tobbio rocks (T_{Max} = 550-600 °C).

627 In summary, reaction (1) remains the only viable mechanism to produce large modes of
628 metamorphic olivine in our samples, implying that substantial modes of brucite were stable
629 throughout prograde subduction until consumption via this reaction. Considering the maximum
630 thermal stability of brucite to 550 °C (Bretscher et al., 2018), all brucite is expected to have
631 reacted out at Erro Tobbio, notably the low X_{Mg} brucite that decomposes at lower temperature
632 in the continuous brucite dehydration reaction. Overall, a prograde reaction path involving
633 reactions (2)-(6) during hydration, (7) during serpentine transformation, and (1) during partial
634 dehydration at intermediate subduction zone depths well explains the petrological and
635 geochemical features of our samples and of serpentinite systems devoid of SiO_2
636 metasomatism. Other subducted serpentinites that do not exhibit significant SiO_2
637 metasomatism (Fig. 4a) and developed notable modes of metamorphic olivine within the
638 antigorite stability field during subduction such as Zermatt and Lago di Cignana (Gilio et al.,
639 2019) likely followed similar reaction paths.

640

641 **5.4. Element inventory of the dehydration veins**

642 The mm to cm-thick veins cross-cutting the Erro Tobbio antigorite serpentinites contain the
643 same metamorphic phases (olivine, Ti-clinohumite, magnetite, diopside, chlorite, antigorite -
644 and retrograde serpentine) as their host rocks. No hydrothermal alteration envelope around

645 the veins can be recognized; hence, the vein-forming fluid can be considered to have been in
646 chemical and thermodynamic equilibrium with the enclosing serpentinites. Our observations
647 (section 5.3) underline the importance of the brucite-out reaction (1) in the studied rocks, in
648 agreement with numerous studies that have investigated mechanical and structural
649 (Scambelluri et al., 1995; Plümper et al., 2017), isotopic (e.g., Früh-Green et al. 2001;
650 Scambelluri and Tonarini, 2012; Halama et al., 2014) and chemical aspects (e.g., Scambelluri
651 et al., 2001 John et al., 2011).

652 Besides the continuous brucite-out reaction, replacement of relict mantle clinopyroxene by
653 metamorphic diopside, Ti-clinohumite, chlorite, and minor magnetite in the wall rocks indicate
654 the progress of another multivariant dehydration reaction producing Ti-clinohumite
655 (Trommsdorff and Evans, 1980), i.e.,

656 Ti-Al Mantle Clinopyroxene + Brucite + Antigorite = Diopside + Ti-chondrodite + Olivine +
657 Chlorite + H_2O (8)

658 Progress of the multivariant reactions (1) and (8) continuously liberated minor fluid pulses
659 derived from different chemical subdomains of the dehydrating system (Plümper et al., 2017)
660 into the developing vein systems, allowing for progressive vein reworking and extensive
661 mineral inter- and overgrowth (Fig. 1c-d, 2e-f). Consequently, modal abundances of the vein-
662 forming minerals are different from those in the wall rocks and highly variable as vein
663 assemblages continuously equilibrate with fluid components derived from nearby dehydration
664 reactions.

665 Bulk vein and vein mineral compositional patterns are generally similar to the wall rocks (Fig.
666 5b), but bulk compositions display highly variable and partly elevated Li, Sr, Y, REE, HFSE
667 and W (+Mo) abundances compared to the host serpentinites. Coupling of Sr, Y, and Dy with
668 CaO bulk rock abundances along a mixing trend with diopside (Fig. 9a), and of Nb, Zr (not
669 shown), and W or Nb with TiO_2 along a mixing trend with Ti-clinohumite (Fig. 9b) reveal that

670 the variable element abundances in the veins are controlled by the variable modes of these
671 mineral repositories in the veins. Similar mineral compositions in veins and wall rocks (Fig. 10)
672 thereby support an internal derivation of vein-forming fluids.

673 The high Sr concentration in vein ETCL4B2-VEIN, which is prominently higher than in the
674 other veins and slightly off-trend for Sr vs. CaO, is associated with the highest P_2O_5 (note the
675 overall positive P anomalies in the veins) and LREE concentrations of all veins and may
676 indicate the presence of apatite in the sampled vein segment. We did not observe any apatite
677 in the thin section, however. Hafnium and Ta, as well as HREEs are concentrated in both,
678 diopside and Ti-clinohumite. HREEs are also significantly incorporated into olivine, thus
679 accounting for elevated HREE abundances in the vein bulks. Prominent vein bulk enrichments
680 in Li indicate loss from the serpentinites (Fig. 5b; see also Fig. 7a), and elevated Li
681 concentrations in metamorphic (Fig. 7a) and vein olivine reveal Li redistribution during the
682 brucite-consuming reaction (1). The effect of retrograde hydration on the bulk trace element
683 signatures of the veins appears to be limited for the elements discussed above since bulk vein
684 concentrations appear to be linked to chemical signatures of the initial prograde vein-forming
685 minerals.

686

687 **5.5. Geodynamic implications**

688 *Rock-buffered serpentinisation environments*

689 Hydration signatures in the Erro Tobbio antigorite serpentinites reveal moderate FME
690 enrichments and isochemical serpentinisation with respect to major elements. A lack of
691 prominent U enrichments (measured Th/U ratios range between 1.6 and 0.3 relative to modern
692 depleted mantle of ~2.5; U/Cs << 1) characteristic of MOR environments (Peters et al., 2017),
693 and alkali enrichments with Rb/Cs of between 4 and 26 are indicative of shallow forearc
694 hydration by early dehydration fluids from clays and altered oceanic crust as well as,

695 subordinately, sedimentary pore fluids (Kahl et al., 2015; Albers et al., in review). Such shallow
696 forearc fluid imprints can potentially be expected in a suprasubduction position (Früh-Green
697 et al., 2001; Scambelluri and Tonarini, 2012; Kahl et al., 2015; Albers et al., in review) or along
698 bend-faults in the down-going slab (Fig. 11; Ranero et al., 2003; Faccenda et al., 2009; John
699 et al., 2011; Kendrick et al., 2011; Halama et al., 2014). In contrast to studies by Früh-Green
700 et al. (2001) and Scambelluri and Tonarini (2012) conducted on another sample suite, we do
701 not observe evidence for ocean water-dominated hydration or geochemical differences
702 between structural domains. Considering the apparent coherency of the Erro Tobbio unit,
703 numerous shear zones (Fig. 1a), and strong fluid localisation on the metre-scale during
704 subduction (Hermann et al., 2000; Früh-Green et al., 2001; Cannaò et al., 2016), such
705 heterogeneity could indicate heterogeneous fluid imprints within the Erro Tobbio unit. The
706 exact position of the Erro Tobbio unit during hydration and subduction remains unclear due to
707 the lack of comparable bend fault serpentinite data and the poorly constrained spatial
708 variability of fluid imprints within the Erro Tobbio unit.

709 Our data on both the geochemistry and petrology of the Erro Tobbio antigorite serpentinites
710 characterise subducted serpentinite that formed close to the hydration front where a rock-
711 buffered hydration environment prevails. This is documented by the incomplete degrees of
712 mantle rock hydration (i.e., mantle relics are common), both on mineral (Fig. 1a, 2a,b) and on
713 rock body scales (e.g., Rampone et al., 2005) and by trace element enrichment patterns (Figs.
714 5a and 8) characteristic of rock-buffered fluid conditions. Such rock-buffered or “isochemical”
715 (for SiO_2) hydration, driven by depleted or dilute fluids and low fluid-rock ratios, might be
716 particularly relevant for deeper sections of hydrated slab mantle (as inferred from geophysical
717 data; Peacock, 2001; Korenaga 2017; Bloch et al., 2018; Cai et al., 2018), and dehydration
718 fronts. Substantial brucite stability within these environments would be consequential and is
719 indeed suggested by geophysical data for the deeper slab (lower seismic zone; Bloch et al.,
720 2018). The magma-poor nature of the Ligurian Ocean, as evidenced by a scarcity of igneous
721 rocks, could further have limited the generation of SiO_2-rich fluids due to a scarcity of SiO_2-

722 richer rocks/sources. To the contrast, fluid-buffered or “non-isochemical” hydration in the
723 upper few 100 metres of the oceanic lithosphere (Fig. 11; Bach et al., 2004; Paulick et al.,
724 2006; Kodolányi et al., 2012; Malvoisin, 2015), commonly considered representative of
725 serpentinised oceanic lithospheric mantle, and along most of the subduction interface
726 (Scambelluri et al., 2014; Cannaò et al., 2015; 2016) appears to be accompanied by pervasive
727 Si metasomatism.

728

729 *Element loss from serpentinites during subduction dehydration*

730 Comparison of reactant and product phase compositions of reactions (1) and (8) for vein-wall
731 rock pairs allows for a qualitative estimate of the dehydration fluid composition. The lack of
732 residual brucite in the antigorite serpentinites does not allow for considering potential brucite
733 contributions in reaction (1), however, data from Kodolányi et al. (2012) suggests that brucite
734 does not incorporate considerable amounts of FMEs. Higher concentrations of Na, Cl, As, Cr,
735 and Ba in matrix antigorite of low-strain domains (Fig. 10a), and of B, Cr, As, Rb, Sb, and Cs
736 in matrix antigorite from high-strain domains (Fig. 10b) compared to the respective
737 metamorphic olivine compositions indicate an effective loss of these elements from the
738 dehydrating serpentinites into the fluid. Few Na- and Cl-rich vein olivine analyses in the high-
739 strain domains are suspicious, however, and we attribute these unusual compositions to sub-
740 microscopic salt or fluid inclusions that could not be resolved optically or in the transient LA-
741 ICP-MS signals. Product phases of reaction (8) contain prominently less Na in general, as well
742 as less Cr, Sb, and Cs in the low-strain domains (Fig. 10c), and less B, As, Rb, and Cs in the
743 high-strain domains (Fig. 10d) compared to the reactants. Strontium and Ba are scavenged
744 by diopside. On grounds of the higher enrichment in alkali and alkaline earth metals in
745 serpentine after pyroxene (section 5.2), reaction (8) that consumes this type of high-Sr-Ba-
746 Rb-Cs antigorite might play an essential role in the cycling of these elements during partial
747 serpentinite dehydration at intermediate depths (Fig. 11).

6. Conclusions

Our geochemical and petrological study of a suite of Erro Tobbio antigorite serpentinites and associated dehydration veins provides new insights into the serpentinisation and subduction history of these rocks. Bulk rock compositions are variably melt-depleted and reveal the absence of significant SiO_2 and CaO addition or loss throughout hydration and dehydration. At mineral scale, preservation of precursor mineral chemical signatures along with low-*T* textural and chemical serpentinisation features reveal limited overprint and chemical disequilibria even at scales of tens of µm. Geochemical and petrological changes of the Erro Tobbio peridotites during serpentinisation and subduction were thus buffered by the initial rock compositions, in contrast to fluid-buffered hydration accompanied by significant SiO_2 metasomatism at, e.g., mid ocean ridges. Fluid-mobile element enrichment patterns with U/Cs << 1 and Rb/Cs of between 4 and 26 thereby fingerprint fluids sourced from early clay or altered oceanic crust dehydration with a minor sedimentary pore fluid component within the shallow forearc as part of the slab or in a suprasubduction position. While hydration imprints are mostly uniform within the studied antigorite serpentinites, it remains unclear whether the same applies to the whole Erro Tobbio unit.

As a consequence of SiO_2-neutral serpentinisation, olivine hydration resulted in pronounced brucite formation. Internal SiO_2 release from orthopyroxene could only compensate for one third of all brucite produced by complete olivine hydration. Serpentine phase transformation without external SiO_2 likely produced even more brucite along with antigorite, before partial dehydration by brucite + antigorite consumption produced up to 40 vol. % of metamorphic olivine and extensive olivine + Ti-clinohumite + magnetite vein networks.

Rock-buffered fluid-rock interactions thus provide a mechanism for stabilising brucite in subduction zone serpentinites, presumably along hydration fronts and within deeper sections

773 of the oceanic lithospheric mantle. Subsequent brucite consumption drives metamorphic
774 olivine formation and partial serpentinite dehydration at temperatures < 550 °C and prior to
775 antigorite breakdown. Fluids released during the olivine-Ti-clinohumite-magnetite-diopside
776 vein-forming reactions in the Erro Tobbio antigorite serpentinites infer effective loss of alkali
777 elements, B, Cr, As, Sb, and Ba from the wall rocks into the plate interface and mantle wedge,
778 and important Sr, REE and HFSE redistribution into vein minerals. Such fluid cycling from
779 hydration to subduction is complementary to that associated with SiO_2-metasomatised and
780 brucite-poor serpentinites formed near the ocean floor, usually considered representative of
781 slab serpentinites.

782

783 Acknowledgements

784 Jörg Hermann and Daniela Rubatto are greatly thanked for the fruitful discussions during
785 manuscript preparation. Calibration and assisting of microprobe measurements by P. Lanari
786 and J. Pape is greatly appreciated. We gratefully acknowledge the thoughtful reviews that
787 helped to better shape our arguments in this manuscript. P. Agard is thanked for the editorial
788 handling of the manuscript. This research has received funding from the People Programme
789 (Marie Curie Actions) of the European Union's Seventh Framework Programme FP7/2017-
790 2013/under REA grant agreement no. 604713, 'Zooming in between Plates (ZIP)'.

791 References

792 Agard P., Yamato P., Soret M., Prigent C., Guillot S., Plunder A., Dubacqa B., Chauvete A.
793 and Monié P. (2016). Plate interface rheological switches during subduction infancy: Control
794 on slab penetration and metamorphic sole formation. Earth and Planetary Science Letters,
795 451, 208-220.

796 Albers E., Kahl W.-A., Beyer L. and Bach W. (2019). Mantle wedge serpentinization traps
797 FMEs: implications for element mobilization at forearc depth from serpentinite mud volcanism
798 (Mariana forearc). Submitted to Lithos.

799 Allen D.E. and Seyfried Jr W.E. (2005). REE controls in ultramafic hosted MOR hydrothermal
800 systems: an experimental study at elevated temperature and pressure. Geochimica et
801 Cosmochimica Acta, 69(3), 675-683.

802 Andreani M., Munoz M., Marcaillou C. and Delacour A. (2013). μXANES study of iron redox
803 state in serpentine during oceanic serpentinization. Lithos, 178, 70-83.

804 Andreani M., Escartin J., Delacour A., Ildefonse B., Godard M., Dyment J., Fallick A.E. and
805 Fouquet Y. (2014). Tectonic structure, lithology, and hydrothermal signature of the Rainbow
806 massif (Mid-Atlantic Ridge 36° 14′ N). Geochemistry, Geophysics, Geosystems, 15(9),
807 3543–3571.

808 Angiboust S., Agard P., Raimbourg H., Yamato P. and Huet B. (2011). Subduction interface
809 processes recorded by eclogite-facies shear zones (Monviso, W. Alps). Lithos, 127(1-2), 222-
810 238.

811 Angiboust S., Kirsch J., Oncken O., Glodny J., Monié P. and Rybacki E. (2015). Probing the
812 transition between seismically coupled and decoupled segments along an ancient subduction
813 interface. Geochemistry, Geophysics, Geosystems, 16(6), 1905-1922.

814 Armstrong J.T. (1995). Citzaf - a package of correction programs for the quantitative Electron
815 Microbeam X-Ray-Analysis of thick polished materials, thin-films, and particles. Microbeam
816 Analysis, 4(3), 177-200

817 Bach W., Garrido C.J., Paulick H., Harvey J. and Rosner M. (2004). Seawater-peridotite
818 interactions: First insights from ODP Leg 209, MAR 15 N. Geochemistry, Geophysics,
819 Geosystems, 5(9).

820 Bach W., Paulick H., Garrido C.J., Ildefonse B., Meurer W.P. and Humphris S.E. (2006).
821 Unraveling the sequence of serpentinization reactions: petrography, mineral chemistry, and
822 petrophysics of serpentinites from MAR 15 N (ODP Leg 209, Site 1274). Geophysical research
823 letters, 33(13).

824 Bali E., Keppler H. and Audetat A. (2012). The mobility of W and Mo in subduction zone fluids
825 and the Mo–W–Th–U systematics of island arc magmas. Earth and Planetary Science Letters,
826 351, 195-207.

827 Becker H., Jochum, K.P. and Carlson R.W. (1999). Constraints from high-pressure veins in
828 eclogites on the composition of hydrous fluids in subduction zones. Chemical
829 Geology, 160(4), 291-308.

830 Bideau D., Hebert R., Hekinian R. and Cannat M. (1991). Metamorphism of deep-seated rocks
831 from the Garrett Ultrafast Transform (East Pacific Rise near 13° 25′ S). Journal of Geophysical
832 Research: Solid Earth 96(B6), 10079–10099.

833 Bloch W., John T., Kummerow J., Salazar P., Krüger O.S. and Shapiro S.A. (2018). Watching
834 Dehydration: Seismic Indication for Transient Fluid Pathways in the Oceanic Mantle of the
835 Subducting Nazca Slab. Geochemistry, Geophysics, Geosystems, 19(9), 3189-3207.

836 Bonifacie M., Busigny V., Mével C., Philippot P., Agrinier P., Jendrzejewski N., Scambelluri M.
837 and Javoy M. (2008). Chlorine isotopic composition in seafloor serpentinites and high-
838 pressure metaperidotites. Insights into oceanic serpentinization and subduction processes.
839 Geochimica et Cosmochimica Acta, 72(1), 126-139.

840 Borghini G., Rampone E., Crispini L., De Ferrari R. and Godard M. (2007). Origin and
841 emplacement of ultramafic–mafic intrusions in the Erro-Tobbio mantle peridotite (Ligurian
842 Alps, Italy). Lithos, 94(1), 210-229.

843 Boschi C., Dini A., Früh-Green G.L. and Kelley D.S. (2008). Isotopic and element exchange
844 during serpentinization and metasomatism at the Atlantis Massif (MAR 30°N): Insights from B
845 and Sr isotope data. Geochimica et Cosmochimica Acta, 72(7), 1801–1823.

846 Bostock M.G., Hyndman R.D., Rondenay S. and Peacock S.M. (2002). An inverted continental
847 Moho and serpentinization of the forearc mantle. Nature, 417(6888), 536.

848 Bretscher A., Hermann J. and Pettke T. (2018). The influence of oceanic oxidation on
849 serpentinite dehydration during subduction. Earth and Planetary Science Letters, 499, 173–
850 184. https://doi.org/10.1016/j.epsl.2018.07.017

851 Brown L., Klein J., Middleton R., Sacks I.S. and Tera F. (1982). ^{10}Be in island-arc volcanoes
852 and implications for subduction. Nature, 299(5885), 718-720.

853 Cai C., Wiens D.A., Shen W. and Eimer M. (2018). Water input into the Mariana subduction
854 zone estimated from ocean-bottom seismic data. Nature, 563(7731), 389.

855 Cannaò E., Agostini S., Scambelluri M., Tonarini S., and Godard M. (2015). B, Sr and Pb
856 isotope geochemistry of high-pressure Alpine metaperidotites monitors fluid-mediated
857 element recycling during serpentinite dehydration in subduction mélange (Cima di Gagnone,
858 Swiss Central Alps). Geochimica et Cosmochimica Acta, 163, 80-100.

859 Cannaò E., Scambelluri M., Agostini S., Tonarini S., and Godard, M (2016). Linking
860 serpentinite geochemistry with tectonic evolution at the subduction plate-interface: The Voltri
861 Massif case study (Ligurian Western Alps, Italy). Geochimica et Cosmochimica Acta, 190,
862 115-133.

863 Chen S., Hin R.C., John T., Brooker R., Ben Bryan, Niu Y. and Elliott T. (2019). Molybdenum
864 systematics of subducted crust record reactive fluid flow from underlying slab serpentine
865 dehydration. Nature Communications, 1–9.

866 Debret B., Nicollet C., Andreani M., Schwartz S. and Godard M. (2013). Three steps of
867 serpentinization in an eclogitized oceanic serpentinization front (Lanzo Massif–Western Alps).
868 Journal of Metamorphic Geology, 31(2), 165-186.

869 De Hoog J.C.M., Hattori K. and Jung H. (2014). Titanium- and water-rich metamorphic olivine
870 in high-pressure serpentinites from the Voltri Massif (Ligurian Alps, Italy): evidence for deep
871 subduction of high-field strength and fluid-mobile elements. Contributions to Mineralogy and
872 Petrology, 167(3), 990. https://doi.org/10.1007/s00410-014-0990-x

873 Deschamps F., Guillot S., Godard M., Chauvel C., Andreani M., and Hattori K. (2010). In situ
874 characterization of serpentinites from forearc mantle wedges: Timing of serpentinization and
875 behavior of fluid-mobile elements in subduction zones. Chemical Geology, 269(3-4), 262–277.

876 Deschamps F., Godard M., Guillot S. and Hattori K. (2013). Geochemistry of subduction zone
877 serpentinites: A review. Lithos, 178, 96–127.

878 Evans B.W. (2004). The serpentinite multisystem revisited: chrysotile is
879 metastable. International Geology Review, 46(6), 479-506.

880 Evans B.W. (2010). Lizardite versus antigorite serpentinite: Magnetite, hydrogen, and life
881 (?). Geology, 38(10), 879-882.

882 Evans B.W., Hattori K. and Baronnet A. (2013). Serpentinite: what, why,
883 where?. Elements, 9(2), 99-106.

884 Faccenda M., Gerya T.V. and Burlini L. (2009). Deep slab hydration induced by bending-
885 related variations in tectonic pressure. Nature Geoscience, 2(11), 790.

886 Frost B.R. and Beard J.S. (2007). On silica activity and serpentinization. Journal of
887 petrology, 48(7), 1351-1368.

888 Früh-Green G.L., Scambelluri M. and Vallis F. (2001). O–H isotope ratios of high pressure
889 ultramafic rocks: implications for fluid sources and mobility in the subducted hydrous mantle.
890 Contributions to Mineralogy and Petrology, 141, 145–159.

891 Fumagalli P. and Poli S. (2004). Experimentally determined phase relations in hydrous
892 peridotites to 6.5 GPa and their consequences on the dynamics of subduction zones. Journal
893 of Petrology, 46(3), 555-578.

894 Garbe-Schönberg C.D. (1993). SIMULTANEOUS DETERMINATION OF THIRTY - SEVEN
895 TRACE ELEMENTS IN TWENTY - EIGHT INTERNATIONAL ROCK STANDARDS BY ICP -
896 MS. Geostandards and Geoanalytical Research, 17(1), 81-97.

897 Garbe-Schönberg D. and Müller S. (2014). Nano-particulate pressed powder tablets for LA-
898 ICP-MS. Journal of Analytical Atomic Spectrometry, 29, 990-1000.

899 Gilio M., Scambelluri M., Agostini S., Godard M., Peters D. and Pettke T. (2019). Petrology
900 and geochemistry of serpentinites associated with the UHP Lago di Cignana Unit (Italian
901 Western Alps). Journal of Petrology, 60(6), 1229-1262.

902 Guillong M., Meier D.L., Allan M.M., Heinrich C.A. and Yardley B.W.D. (2008). SILLS: A
903 MATLAB-based program for the reduction of laser ablation ICP-MS data of homogeneous
904 materials and inclusions. In: Sylvester P. (ed.), Laser ablation ICP-MS in the Earth sciences:
905 Current practices and outstanding issues. Mineralogical Association of Canada Short Course
906 Series, 40, 328–333.

907 Guillot S., Hattori K.H., de Sigoyer J., Nägler, T. and Auzende A.-L. (2001). Evidence of
908 hydration of the mantle wedge and its role in the exhumation of eclogites. Earth and Planetary
909 Science Letters, 193(1–2), 115–127.

910 Hacker B.R., Peacock S.M., Abers G.A. and Holloway S.D. (2003). Subduction factory 2. Are
911 intermediate-depth earthquakes in subducting slabs linked to metamorphic dehydration
912 reactions?. Journal of Geophysical Research: Solid Earth, 108(B1), 1-16.

913 Halama R., Bebout G.E., John T. and Scambelluri M. (2014). Nitrogen recycling in subducted
914 mantle rocks and implications for the global nitrogen cycle. International Journal of Earth
915 Sciences, 103(7), 2081-2099.

916 Halter W.E., Pettke T., Heinrich C.A. and Rothen-Rutishauser B. (2002). Major to trace
917 element analysis of melt inclusions by laser ablation ICP-MS: methods of quantification.
918 Chemical Geology, 183, 63-86.

919 Harvey J., Savov I.P., Agostini S., Cliff R.A. and Walshaw R. (2014). Si-metasomatism in
920 serpentinized peridotite: the effects of talc-alteration on strontium and boron isotopes in
921 abyssal serpentinites from Hole 1268a, ODP Leg 209. Geochimica et Cosmochimica
922 Acta, 126, 30-48.

923 Hattori K.H. and Guillot S. (2003). Volcanic fronts form as a consequence of serpentinite
924 dehydration in the forearc mantle wedge. Geology, 31(6), 525-528.

925 Hattori K.H. and Guillot S. (2007). Geochemical character of serpentinites associated with
926 high - to ultrahigh - pressure metamorphic rocks in the Alps, Cuba, and the Himalayas:
927 Recycling of elements in subduction zones. Geochemistry, Geophysics, Geosystems, 8(9), 1-
928 27.

929 Hermann J., Müntener O. and Scambelluri M. (2000). The importance of serpentinite mylonites
930 for subduction and exhumation of oceanic crust. Tectonophysics, 327(3), 225-238.

931 Hoogerduijn Strating E.H., Rampone E., Piccardo G.B., Drury M.R. and Vissers R.L.M. (1993).
932 Subsolidus emplacement of mantle peridotites during incipient oceanic rifting and opening of
933 the Mesozoic Tethys (Voltri Massif, NW Italy). Journal of Petrology, 34(5), 901-927.

934 Hulme S. M., Wheat C.G., Fryer P. and Mottl M. J. (2010). Pore water chemistry of the Mariana
935 serpentinite mud volcanoes: a window to the seismogenic zone. Geochemistry, Geophysics,
936 Geosystems, 11(1).

937 Hyndman R.D. and Peacock S.M. (2003). Serpentinization of the forearc mantle. Earth and
938 Planetary Science Letters, 212(3-4), 417-432.

939 Incel S., Hilairet N., Labrousse L., John T., Deldicque D., Ferrand T., Wang Y., Renner J.,
940 Morales L. and Schubnel A. (2017). Laboratory earthquakes triggered during eclogitization of
941 lawsonite-bearing blueschist. Earth and Planetary Science Letters, 459, 320-331.

942 John T., Scherer E.E., Haase K. and Schenk, V. (2004). Trace element fractionation during
943 fluid-induced eclogitization in a subducting slab: trace element and Lu–Hf–Sm–Nd isotope
944 systematics. Earth and Planetary Science Letters, 227(3-4), 441-456.

945 John T., Klemd R., Gao J. and Garbe-Schönberg C.D. (2008). Trace-element mobilization in
946 slabs due to non steady-state fluid–rock interaction: constraints from an eclogite-facies
947 transport vein in blueschist (Tianshan, China). Lithos, 103(1), 1-24.

948 John T., Scambelluri M., Frische M., Barnes J.D. & Bach W. (2011). Dehydration of subducting
949 serpentinite: Implications for halogen mobility in subduction zones and the deep halogen cycle.
950 Earth Planetary Science Letters, 308(1-2), 65–76.

951 John T., Gussone N., Podladchikov Y.Y., Bebout G.E., Dohmen R., Halama R., Klemd R.,
952 magna T. and Seitz H.M. (2012). Volcanic arcs fed by rapid pulsed fluid flow through
953 subducting slabs. Nature Geoscience, 5(7), 489.

954 Kahl W.A., Jöns N., Bach W., Klein F. and Alt J.C. (2015). Ultramafic clasts from the South
955 Chamorro serpentine mud volcano reveal a polyphase serpentinization history of the Mariana
956 forearc mantle. Lithos, 227, 1-20.

957 Kempf E.D. and Hermann J. (2018). Hydrogen incorporation and retention in metamorphic
958 olivine during subduction: Implications for the deep water cycle. Geology, 46(6), 571-574.

959 Kendrick M.A., Scambelluri M., Honda M. and Phillips D. (2011). High abundances of noble
960 gas and chlorine delivered to the mantle by serpentinite subduction. Nature Geoscience,
961 4(11), 807–812.

962 Kendrick M.A., Honda M., Pettke T., Scambelluri M. and Phillips D. (2013). Halogen and noble
963 gas systematics of ocean floor and ophiolitic serpentinites: implications for global volatile
964 recycling. Earth and Planetary Science Letter, 365, 86-96.

965 Kessel R., Schmidt M.W., Ulmer P. and Pettke T. (2005). Trace element signature of
966 subduction-zone fluids, melts and supercritical liquids at 120–180 km
967 depth. Nature, 437(7059), 724.

968 Klein F., Bach W., Jöns N., McCollom T., Moskowitz B. and Berquó T., 2009. Iron partitioning
969 and hydrogen generation during serpentinization of abyssal peridotites from 15 N on the Mid-
970 Atlantic Ridge. Geochimica et Cosmochimica Acta, 73(22), pp.6868-6893.

971 Klein F., Bach W., Humphris S.E., Kahl W.A., Jöns N., Moskowitz B. and Berquó T.S. (2014).
972 Magnetite in seafloor serpentinite—Some like it hot. Geology, 42(2), 135-138.

973 Kodolányi J. and Pettke T. (2011). Loss of trace elements from serpentinites during fluid-
974 assisted transformation of chrysotile to antigorite—An example from Guatemala. Chemical
975 Geology, 284(3), 351-362.

976 Kodolányi J., Pettke T., Spandler C., Kamber B.S. and Gmeling K. (2012). Geochemistry of
977 Ocean Floor and Fore-arc Serpentinites: Constraints on the Ultramafic Input to Subduction
978 Zones. Journal of Petrology, 53(2), 235–270.

979 Korenaga J. (2017). On the extent of mantle hydration caused by plate bending. Earth and
980 Planetary Science Letters, 457, 1-9.

981 Lafay R., Deschamps F., Schwartz S., Guillot S., Godard M., Debret B., and Nicollet C. (2013).
982 High-pressure serpentinites, a trap-and-release system controlled by metamorphic conditions:
983 Example from the Piedmont zone of the western Alps. Chemical Geology, 343, 38-54.

984 Leach A.M. and Hieftje G.M. (2000). Methods for shot-to-shot normalization in laser ablation
985 with an inductively coupled plasma time-of-flight mass spectrometer. Journal of Analytical
986 Atomic Spectrometry, 15(9), 1121– 1124.

987 Malvoisin B. (2015). Mass transfer in the oceanic lithosphere: serpentinization is not
988 isochemical. Earth and Planetary Science Letters, 430, 75-85.

989 Marschall H.R. and Schumacher J.C. (2012). Arc magmas sourced from mélange diapirs in
990 subduction zones. Nature Geoscience, 5(12), 862.

991 Niu Y. (2004). Bulk-rock Major and Trace Element Compositions of Abyssal Peridotites:
992 Implications for Mantle Melting, Melt Extraction and Post-melting Processes Beneath Mid-
993 Ocean Ridges. Journal of Petrology, 45(12), 2423–2458.

994 Peacock S.M. (2001). Are the lower planes of double seismic zones caused by serpentine
995 dehydration in subducting oceanic mantle?. Geology, 29(4), 299-302.

996 Padrón-Navarta J.A., Sánchez-Vizcaíno V.L., Hermann J., Connolly J.A., Garrido C.J.,
997 Gómez-Pugnaire M.T. and Marchesi C. (2013). Tschermak's substitution in antigorite and
998 consequences for phase relations and water liberation in high-grade
999 serpentinites. Lithos, 178, 186-196.

1000 Palme H. and O'Neill H.S.C. (2014). Cosmochemical estimates of mantle composition. In:
1001 Holland, H., Turekian, K. (Eds.), Treatise on Geochemistry, second ed. 3. Elsevier- Pergamon,
1002 Oxford, pp. 1–39.

1003 Paulick H., Bach W., Godard M., De Hoog J.C.M. Suhr, G. and Harvey J. (2006).
1004 Geochemistry of abyssal peridotites (mid-Atlantic ridge, 15° 20′ N, ODP leg 209):
1005 implications for fluid/rock interaction in slow spreading environments. Chemical Geology 234
1006 (3–4), 179–210.

1007 Peters D. and Pettke T. (2017). Evaluation of Major to Ultra Trace Element Bulk Rock
1008 Chemical Analysis of Nanoparticulate Pressed Powder Pellets by LA - ICP - MS.
1009 Geostandards and Geoanalytical Research, 41(1), 5-28.

1010 Peters D., Bretscher A., John T., Scambelluri M. and Pettke T. (2017). Fluid-mobile Elements
1011 in Serpentinites: Constraints on Serpentinisation Environments and Element Cycling in
1012 Subduction Zones. Chemical Geology, 466, 654-666.

1013 Pettke T., Oberli F., Audétat A., Guillong M., Simon A.C., Hanley J.J. and Klemm L.M. (2012).
1014 Recent developments in element concentration and isotope ratio analysis of individual fluid
1015 inclusions by laser ablation single and multiple collector ICP-MS. Ore Geology Reviews, 44,
1016 10-38.

1017 Philippot P., Busigny V., Scambelluri M. and Cartigny P. (2007). Oxygen and nitrogen isotopes
1018 as tracers of fluid activities in serpentinites and metasediments during subduction. Mineralogy
1019 and Petrology, 91(1), 11-24.

1020 Piccardo G.B. and Vissers R.L.M. (2007). The pre-oceanic evolution of the Erro-Tobbio
1021 peridotite (Voltri Massif, Ligurian Alps, Italy). Journal of Geodynamics, 43(4), 417-449.

1022 Plümper O., John T., Podladchikov Y.Y., Vrijmoed J.C., and Scambelluri M. (2017). Fluid
1023 escape from subduction zones controlled by channel-forming reactive porosity. Nature
1024 Geoscience, 10(2), 150-156.

1025 Rampone E., Romairone A. and Hofmann A.W. (2004). Contrasting bulk and mineral
1026 chemistry in depleted mantle peridotites: evidence for reactive porous flow. Earth Planetary
1027 Science Letters, 218(3-4), 491–506.

1028 Rampone E., Romairone A., Abouchami W., Piccardo G.B. and Hofmann A.W. (2005).
1029 Chronology, petrology and isotope geochemistry of the Erro–Tobbio peridotites (Ligurian Alps,
1030 Italy): records of Late Palaeozoic lithospheric extension. Journal of Petrology, 46(4), 799-827.

1031 Ranero C.R., Morgan J.P., McIntosh K. and Reichert C. (2003). Bending-related faulting and
1032 mantle serpentinization at the Middle America trench. Nature, 425(6956), 367.

1033 Scambelluri M., Strating E.H.H., Piccardo G.B., Vissers R.L.M. and Rampone E. (1991).
1034 Alpine olivine- and titanian clinohumite-bearing assemblages in the Erro-Tobbio peridotite
1035 (Voltri Massif, NW Italy). J. Metamorph. Geol. 9 (1), 79–91.

1036 Scambelluri M., Müntener O., Hermann J., Piccardo G.B. and Trommsdorff V. (1995).
1037 Subduction of water into the mantle: history of an Alpine peridotite. Geology, 23(5), 459-462.

1038 Scambelluri M., Piccardo G.B., Philippot P., Robbiano A. and Negretti L. (1997). High salinity
1039 fluid inclusions formed from recycled seawater in deeply subducted alpine serpentinite. Earth
1040 and Planetary Science Letters, 148(3-4), 485-499.

1041 Scambelluri M. and Philippot P. (2001). Deep fluids in subduction zones. Lithos, 55(1-4), 213-
1042 227.

1043 Scambelluri M., Rampone E. and Piccardo G.B. (2001). Fluid and element cycling in
1044 subducted serpentinite: A trace-element study of the Erro-Tobbio high-pressure ultramafites
1045 (Western alps, NW Italy). Journal of Petrology, 42(1), 55–67.

1046 Scambelluri M., Müntener O., Ottolini L., Pettke T. and Vannucci R. (2004). The fate of B, Cl
1047 and Li in the subducted oceanic mantle and in the antigorite breakdown fluids. Earth Planetary
1048 Science Letters, 222(1), 217–234.

1049 Scambelluri M. and Tonarini S. (2012). Boron isotope evidence for shallow fluid transfer across
1050 subduction zones by serpentinized mantle. Geology, 40(10), 907–910.

1051 Scambelluri M., Pettke T., Rampone E., Godard M. and Reusser E. (2014). Petrology and
1052 Trace Element Budgets of High-pressure Peridotites Indicate Subduction Dehydration of
1053 Serpentinized Mantle (Cima di Gagnone, Central Alps, Switzerland). Journal of Petrology,
1054 55(3), 459–498.

1055 Schwarzenbach E.M., Caddick M.J., Beard J.S. and Bodnar R.J. (2016). Serpentinization,
1056 element transfer, and the progressive development of zoning in veins: evidence from a
1057 partially serpentinized harzburgite. Contributions to Mineralogy and Petrology, 171(1), 5.

1058 Schwarzenbach E.M., Caddick M.J., Petroff M., Gill B.C., Cooperdock E.H.G. and Barnes J.D.
1059 (2018) Sulphur and carbon cycling in the subduction zone mélange. Scientific Reports 8,
1060 15517.

1061 Snow, J. E., & Dick, H. J. B. (1995). Pervasive magnesium loss by marine weathering of
1062 peridotite. Geochimica et Cosmochimica Acta, 59(20), 4219–4235.

1063 Spandler C. and Pirard C. (2013). Element recycling from subducting slabs to arc crust: A
1064 review. Lithos, 170, 208-223.

1065 Taetz S., John T., Bröcker M., Spandler C. and Stracke, A. (2018). Fast intraslab fluid-flow
1066 events linked to pulses of high pore fluid pressure at the subducted plate interface. Earth and
1067 Planetary Science Letters, 482, 33-43.

1068 Toft P.B., Arkani-Hamed J. and Haggerty S.E. (1990). The effects of serpentinization on
1069 density and magnetic susceptibility: a petrophysical model. Physics of the Earth and Planetary
1070 Interiors, 65(1-2), 137-157.

1071 Trommsdorff V. and Evans B. W. (1980). Titanian hydroxyl-clinohumite: formation and
1072 breakdown in antigorite rocks (Malenco, Italy). Contributions to Mineralogy and Petrology,
1073 72(3), 229-242.

1074 Ulmer P. and Trommsdorff V. (1995). Serpentine Stability to Mantle Depths and Subduction-
1075 Related Magmatism. Science, 268(5212), 858–861.

1076 Vils F., Pelletier L., Kalt A., Müntener O. and Ludwig T. (2008). The Lithium, Boron and
1077 Beryllium content of serpentinized peridotites from ODP Leg 209 (Sites 1272A and 1274A):
1078 Implications for lithium and boron budgets of oceanic lithosphere. Geochimica et
1079 Cosmochimica Acta, 72(22), 5475–5504.

1080 Wunder B. and Schreyer W., (1997). Antigorite: High pressure stability in the system MgO-
1081 SiO2-H2O (MSH). Lithos 41, 213-227.

1082 Zack T. and John T. (2007). An evaluation of reactive fluid flow and trace element mobility in
1083 subducting slabs. Chemical Geology, 237(1–2), 5–22.

Figure captions

Figure 1 Schematic geological maps of the Erro Tobbio unit including sample locations of this study: a) modified after Vissers et al. (1991) and b) modified after Scambelluri et al. (1995).

Figure 2 Petrographic images of the Erro Tobbio high-strain antigorite serpentinites and cross-cutting dehydration veins: **a)** Partially serpentinised and internally deformed relict mantle clinopyroxene (Cpx_1) porphyroclast in a fine-grained foliated metamorphic matrix of antigorite (Atg_2) + olivine (Ol_2) + magnetite (Mag_2). **b)** Metamorphic olivine porphyroblast (Ol_2) in fine-grained antigorite (Atg_2) + olivine (Ol_2) + magnetite (Mag_2) matrix. **c)** Apparent overgrowth of vein olivine (Ol_V) by vein Ti-clinohumite (Ti-Chu_V) in back-scattered electron image (BSE) and in plane polarised light (PPL); note the zonation in the BSE image, the magnetite inclusions, and that crystal fractures continue from Ol_V into Ti-Chu_V. **d)** Sheared olivine (Ol_V) + Ti-clinohumite (Ti-Chu_V) + magnetite (Mag_V) vein with crack-filling of fine-grained diopside (Di_V).

Figure 3 Petrographic images of the Erro Tobbio low-strain antigorite serpentinites and cross-cutting dehydration veins: **a)** Relict mesh textures with mantle olivine in mesh centres (Ol_1; highlighted with purple lines) and metamorphic antigorite (Atg_2) and olivine (Ol_2) grown along the former serpentine mesh; **b)** Partially hydrated relic mantle clinopyroxene (Cpx_1; EPMA measurement spots ET08-16-W-36 and ET08-16-W-44 in supplementary material 2) replaced by chlorite (Chl_2), magnetite (Mag_2), Ti-clinohumite (Ti-Chu_2), along with minor metamorphic diopside and antigorite (too small to be indicated). **c)** Mantle orthopyroxene (Opx_1) bastite containing fine-grained metamorphic diopside (Di_2) and olivine (Ol_2). **d)** Alteration pseudomorph after spinel with magnetite (Mag_2) in the core surrounded by a chlorite (Chl_2) corona. **e)** Vein Ti-clinohumite (Ti-Chu_V) pierced by diopside needles (Di_V). **f)** Close-up of **e)** displaying intergrowth of diopside (Di_V) and chlorite (Chl_V) with interspersed magnetite (Mag_V) and strongly serpentinised olivine (serp. Ol).

Figure 4 Geochemical characteristics of the Erro Tobbio antigorite serpentinites with **a)** bulk rock MgO/SiO_2 vs. Al_2O_3/SiO_2 (Data for mid ocean ridge (MOR) serpentinites (serp.) from compilation in Peters et al. (2017), for subducted slab serpentinites from Debret et al. (2013; Lanzo) and Gilio et al. (2019; Zermatt-Saas; Lago di Cignana), and for subduction channel serpentinites from Scambelluri et al. (2014; Cima di Gagnone) and Cannaò et al. (2016; Voltri). Note that all Erro Tobbio samples plot atop the terrestrial array, thus implying that their SiO_2-MgO-Al_2O_3 contents were not significantly modified upon hydration. **b)** bulk rock Al_2O_3 vs. CaO, **c)** primitive mantle (PM)-normalised rare earth element patterns for bulk rock data with shaded fields of spinel peridotite and mantle clinopyroxene data for Erro Tobbio from Rampone et al. (2004, 2005), and **d)** bulk rock and clinopyroxene contents of Ce, Gd, and Yb vs. CaO. Data from supplementary materials 1 and 3. Primitive mantle values after Palme and O'Neill (2014). Abbreviations: AS (hs) = antigorite serpentinite (high-strain); AS (ls) = antigorite serpentinite (low-strain), and relict mantle clinopyroxene (Cpx_1)).

Figure 5 Primitive mantle normalised bulk rock trace element distribution diagrams, illustrating fluid-mobile element enrichments in **a)** the Erro Tobbio antigorite (atg) serpentinites, and **b)** associated dehydration veins (data from supplementary material 1). The grey band visualises the apparent melt depletion trend in **a)**. Primitive mantle (PM) values after Palme and O'Neill (2014).

Figure 6 Mineral compositional characteristics for **a)** X_{Mg} vs. MnO and **b)** MnO vs. B in olivine (ol; all analyses), and **c)** V vs. Cr and **d)** bulk-normalised Yb vs. Dy in antigorite (Atg_2) from the Erro Tobbio low- and high-strain antigorite serpentinites. Data points comprise EPMA data from supplementary material 2 in **a**, and LA-ICP-MS data in **a**-**d** from supplementary material 3. Grey-shaded fields of mantle relicts of olivine (Ol_1), orthopyroxene (Opx_1; measured on relict mantle orthopyroxene in a retrogradely overprinted serpentinised dunite from Erro Tobbio) and clinopyroxene (Cpx_1) compositions include data from supplementary material 3 and Rampone et al. (2005). The red-shaded area in **d)** displays the limits of detection (LODs) for

several measurements of antigorite after olivine that did not yield significant concentrations (LOD variability stems from variable laser spot sizes between measurements).

Figure 7 Fluid mobile element enrichment distribution plots in the rock-forming silicates and bulk rocks (data from supplementary materials 1 and 3) for **a)** Li, **b)** B, **c)** Sr, **d)** Ba, **e)** Rb, **f)** Cs, **g)** As, and **h)** Sb. Abbreviations: Ol_1 = mantle olivine; Cpx_1 = mantle clinopyroxene; Opx_1 = mantle orthopyroxene; Atg_2 = metamorphic antigorite; after Ol_1 = metamorphic antigorite (Atg_2) after mantle olivine (Ol_1) ; after Px_1 = metamorphic antigorite (Atg_2)/chlorite (Chl_2) after mantle clino- (Cpx_1) or orthopyroxene (Opx_1); after Spl_1 = metamorphic chlorite after mantle spinel$_1$; Ol_2 = metamorphic olivine; Ti-Chu_2 = metamorphic Ti-clinohumite; < LOD = below limits of detection. Note that Opx_1 reference data were measured on relict mantle orthopyroxene in a retrogradely overprinted serpentinised dunite from Erro Tobbio.

Figure 8 Fluid-mobile element enrichment characteristics in the Erro Tobbio antigorite serpentinites (AS) and antigorite (Atg_2) and chlorite (Chl_2) for **a)** Cl vs. X_{Mg} with bulk rock Cl concentrations (shown as bars) from John et al. (2011), **b)** Sr vs. CaO (bulk-rock normalised), **c)** B vs. Sr, and **d)** Rb vs. Cs including bulk rock data for Erro Tobbio, mid ocean ridge (MOR) and forearc (FA) serpentinites (Peters et al., 2017), and mineral data for serpentine mud from South Chamorro (Kahl et al., 2015). Data taken from supplementary materials 1-3. Abbreviations: after Ol_1 = metamorphic antigorite after mantle olivine (Ol_1) ; after Px_1 = metamorphic antigorite (Atg_2)/chlorite (Chl_2) after mantle clino- (Cpx_1) or orthopyroxene (Opx_1); after Spl_1 = metamorphic chlorite after mantle spinel$_1$.

Figure 9 Trace element patterns in high-pressure dehydration veins in the Erro Tobbio antigorite (Atg) serpentinites for **a)** Sr, Y, and Dy vs. CaO in vein bulks and diopside (Di_v), and b) Nb, W, and Ta in vein bulks and Ti-clinohumite (Ti-Chu_v) . Abbreviations: hs = high-strain; ls = low-strain.

Figure 10 Selected trace element inventories in reactant and product phases for the dehydration reactions brucite-consumption (a, b) and Ti-clinohumite-in (c, d). Ellipses indicate effective element loss into the liberated fluid. Data taken from supplementary materials 2 and 3. Olivine analyses with Na_2O > 0.04 wt. % and Cl > 0.1 wt. % in the high-strain domains were not considered (see text). * = upper concentration limit as lower limit < limit of detection for the respective phase (LOD).

Figure 11 Sketch depicting expected characteristic FME imprints and major element compositional changes during hydration and partial dehydration in **a)** mid-ocean ridge, **b)** shallow forearc, and **c)** deeper forearc settings. Brucite consumption curve given in **c)** for reference. Potential hydration environments of the Erro Tobbio unit are indicated in **b)**, and dehydration fluid compositions related to brucite consumption are in listed in **c)**.

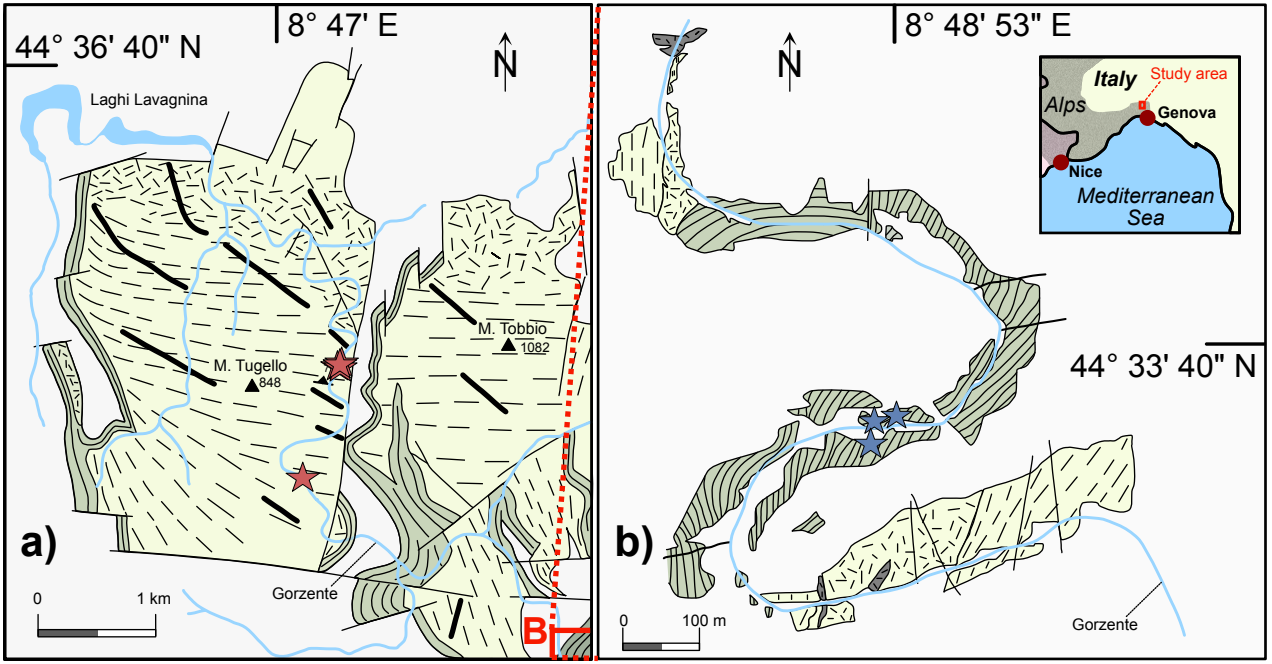

undifferentiated peridotite

granular peridotite

peridotite tectonite

variably serpentinised low-strain peridotite/ serpentinite

low-strain antigorite serpentinite sample

high-strain antigorite serpentinite

pyroxenite layer

metagabbro

high-strain antigorite serpentinite sample

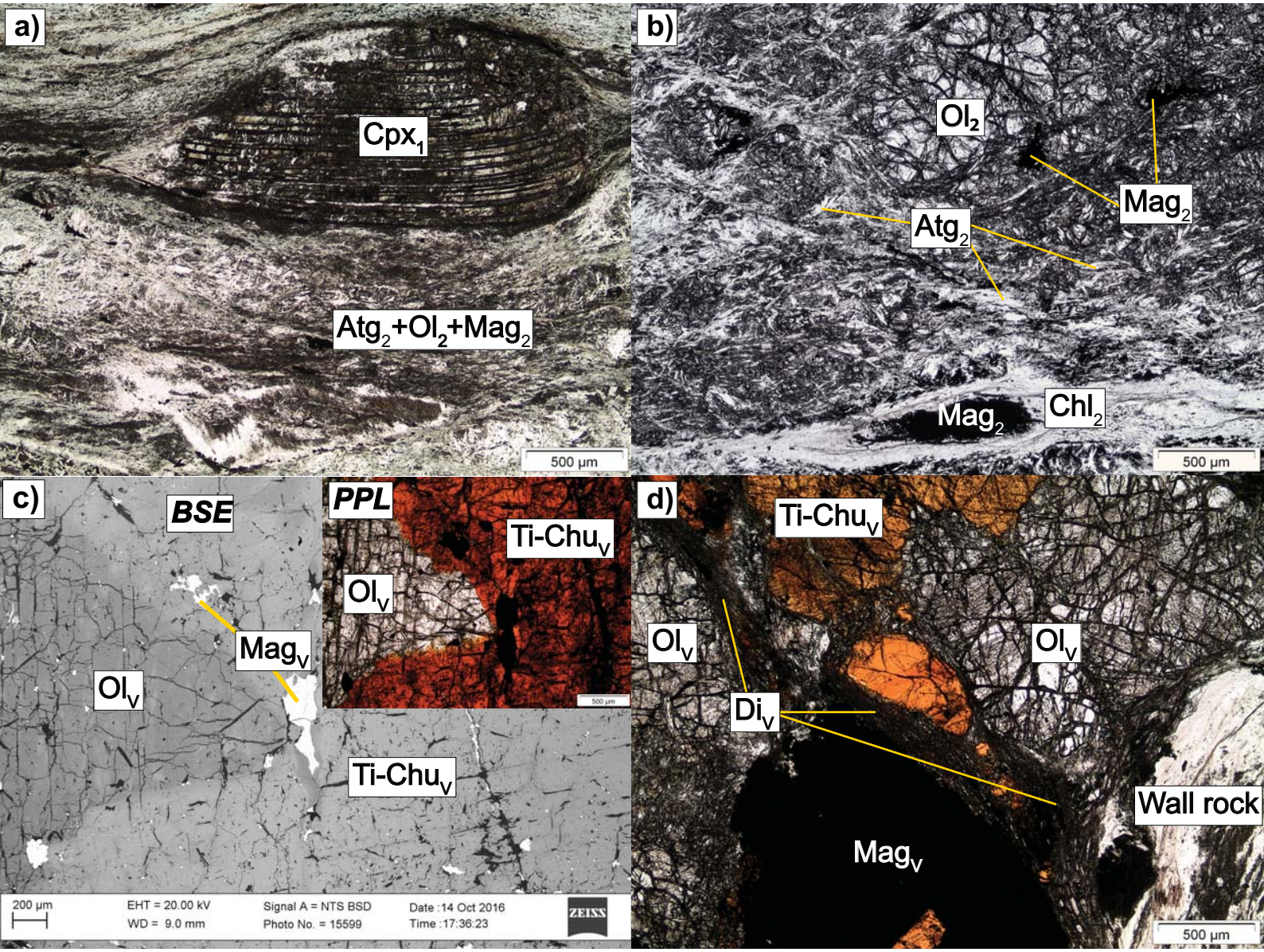
a)
Cpx1
Atg2+Ol2+Mag2
500 µm
b)
Ol2
Mag2
Atg2
Mag2
Chl2
500 µm
c)
BSE
Magv
Olv
PPL
Ti-Chuv
Olv
500 µm
Ti-Chuv
200 µm
EHT = 20.00 kV
WD = 9.0 mm
Signal A = NTS BSD
Photo No. = 15599
Date :14 Oct 2016
Time :17:36:23
ZEISS
d)
Ti-Chuv
Olv
Olv
Div
Wall rock
Magv
500 µm

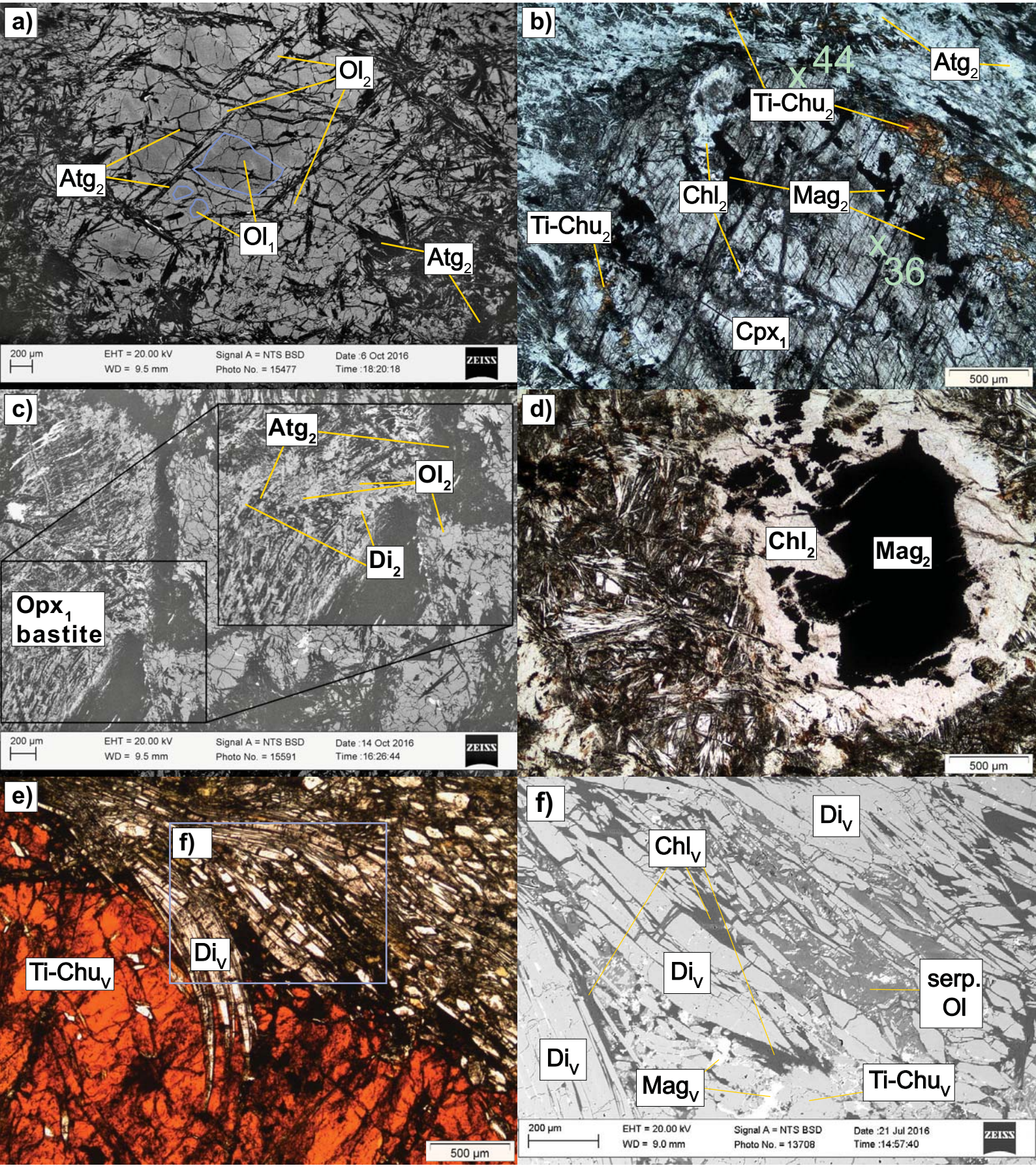
a)
Ol2
Atg2
Ol1
Atg2
200 µm
EHT = 20.00 kV
WD = 9.5 mm
Signal A = NTS BSD
Photo No. = 15477
Date :6 Oct 2016
Time :18:20:18
ZEISS
b)
x44
Atg2
Ti-Chu2
Chl2
Mag2
Ti-Chu2
x36
Cpx1
500 µm
c)
Atg2
Ol2
Di2
Opx1
bastite
200 µm
EHT = 20.00 kV
WD = 9.5 mm
Signal A = NTS BSD
Photo No. = 15591
Date :14 Oct 2016
Time :16:26:44
ZEISS
d)
Chl2
Mag2
500 µm
e)
f)
Ti-Chuv
Div
500 µm
f)
Div
Chlv
Div
serp.
Ol
Div
Magv
Ti-Chuv
200 µm
EHT = 20.00 kV
WD = 9.0 mm
Signal A = NTS BSD
Photo No. = 13708
Date :21 Jul 2016
Time :14:57:40
ZEISS

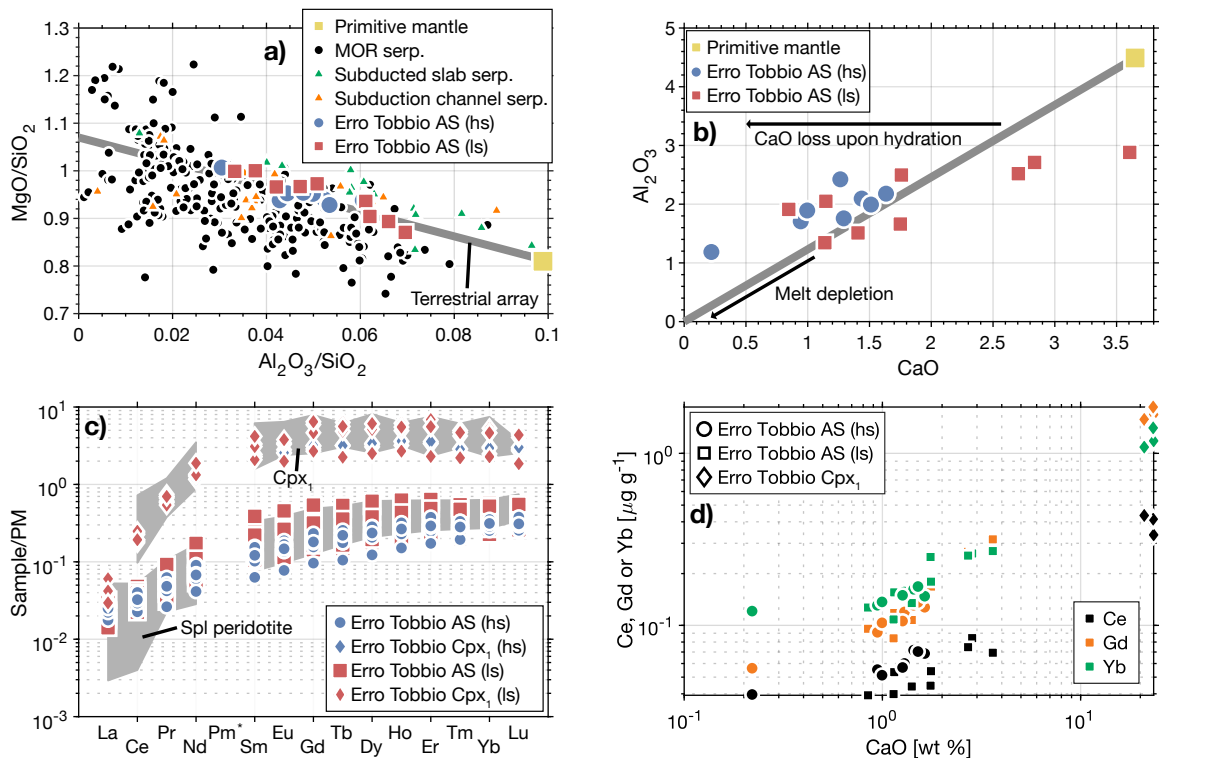
a)
Primitive mantle
MOR serp.
Subducted slab serp.
Subduction channel serp.
Erro Tobbio AS (hs)
Erro Tobbio AS (ls)
Terrestrial array
MgO/SiO2
Al2O3/SiO2
b)
Primitive mantle
Erro Tobbio AS (hs)
Erro Tobbio AS (ls)
CaO loss upon hydration
Melt depletion
Al2O3
CaO
c)
Cpx1
Spl peridotite
Erro Tobbio AS (hs)
Erro Tobbio Cpx1 (hs)
Erro Tobbio AS (ls)
Erro Tobbio Cpx1 (ls)
Sample/PM
La Ce Pr Nd Pm* Sm Eu Gd Tb Dy Ho Er Tm Yb Lu
d)
Erro Tobbio AS (hs)
Erro Tobbio AS (ls)
Erro Tobbio Cpx1
Ce
Gd
Yb
Ce, Gd or Yb [μg g-1]
CaO [wt %]

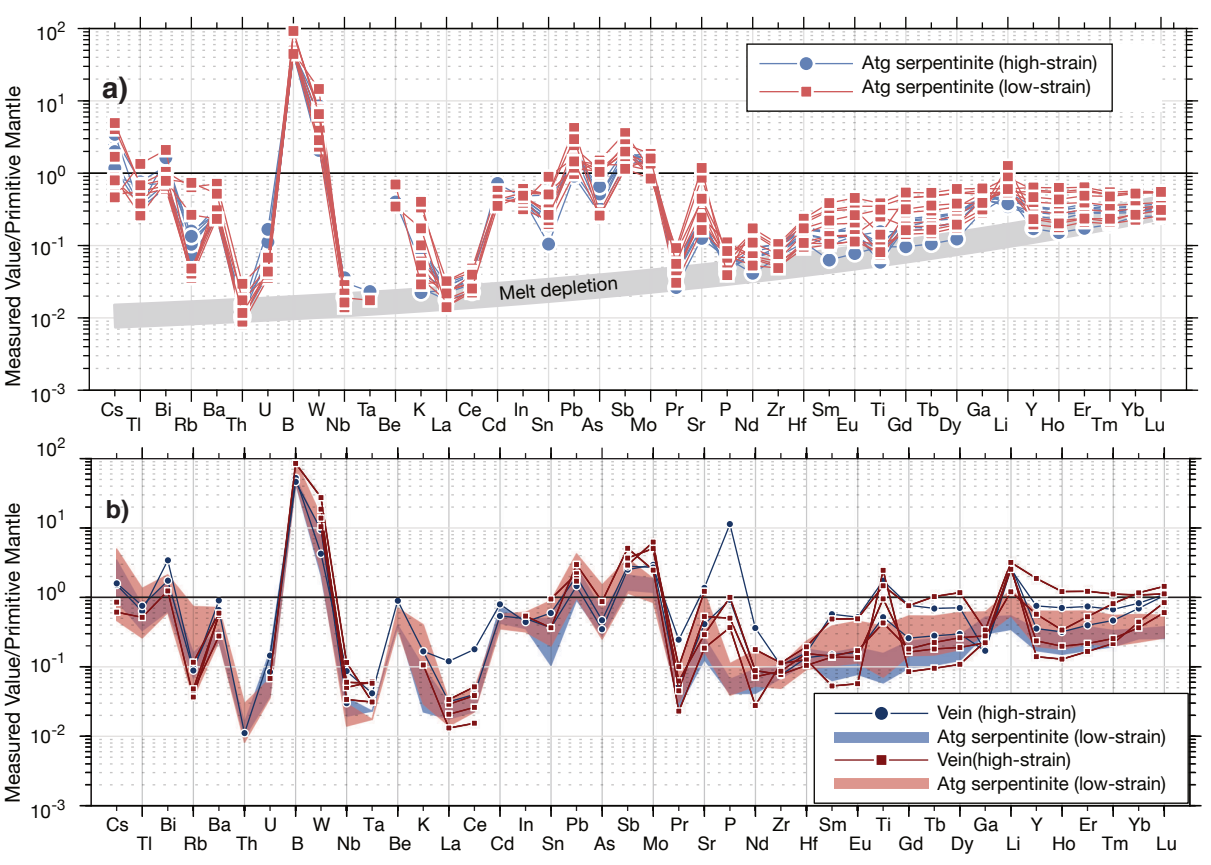
a)
Atg serpentinite (high-strain)
Atg serpentinite (low-strain)
Melt depletion
Measured Value/Primitive Mantle
10^2
10^1
10^0
10^{-1}
10^{-2}
10^{-3}
Cs Tl Bi Rb Ba Th U B W Nb Ta Be K La Ce Cd In Sn Pb As Sb Mo Pr Sr P Nd Zr Hf Sm Eu Ti Gd Tb Dy Ga Li Y Ho Er Tm Yb Lu
b)
Vein (high-strain)
Atg serpentinite (low-strain)
Vein(high-strain)
Atg serpentinite (low-strain)
Measured Value/Primitive Mantle
Cs Tl Bi Rb Ba Th U B W Nb Ta Be K La Ce Cd In Sn Pb As Sb Mo Pr Sr P Nd Zr Hf Sm Eu Ti Gd Tb Dy Ga Li Y Ho Er Tm Yb Lu

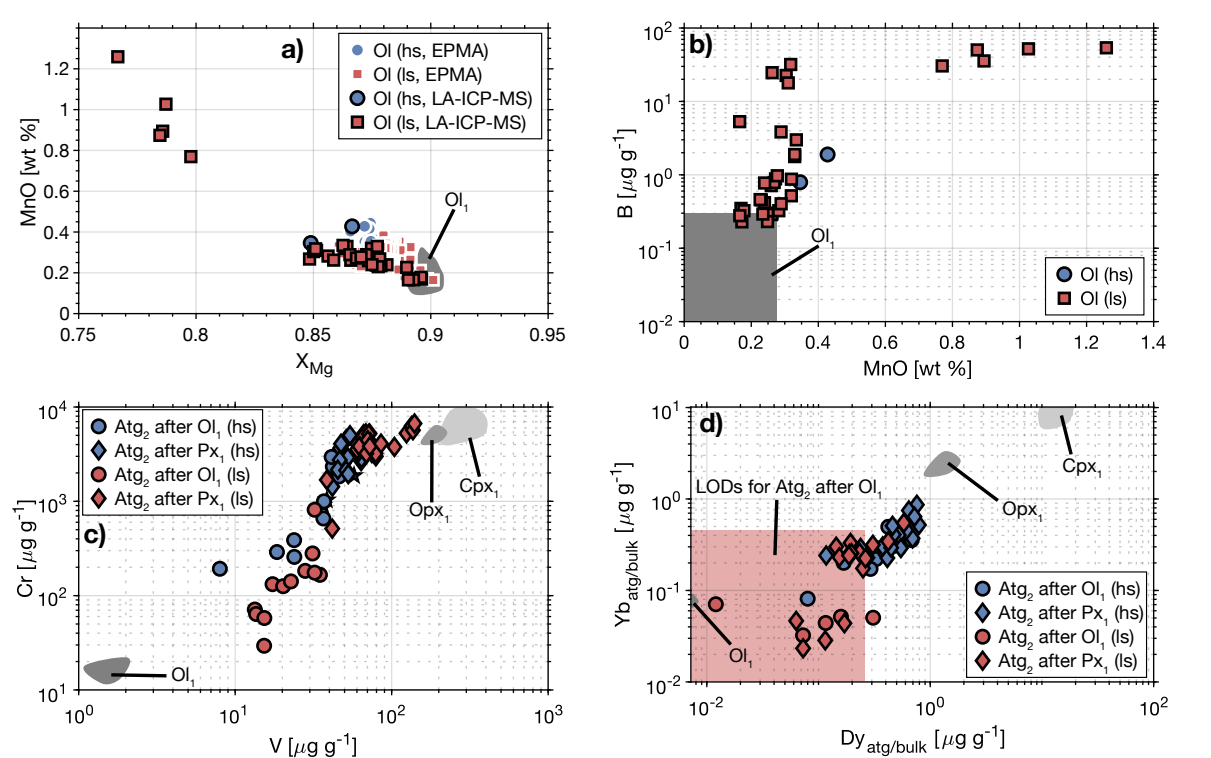
a)
Ol (hs, EPMA)
Ol (ls, EPMA)
Ol (hs, LA-ICP-MS)
Ol (ls, LA-ICP-MS)
Ol1
MnO [wt %]
XMg
b)
Ol (hs)
Ol (ls)
Ol1
B [μg g-1]
MnO [wt %]
c)
Atg2 after Ol1 (hs)
Atg2 after Px1 (hs)
Atg2 after Ol1 (ls)
Atg2 after Px1 (ls)
Cpx1
Opx1
Ol1
Cr [μg g-1]
V [μg g-1]
d)
LODs for Atg2 after Ol1
Cpx1
Opx1
Ol1
Atg2 after Ol1 (hs)
Atg2 after Px1 (hs)
Atg2 after Ol1 (ls)
Atg2 after Px1 (ls)
Yb atg/bulk [μg g-1]
Dy atg/bulk [μg g-1]

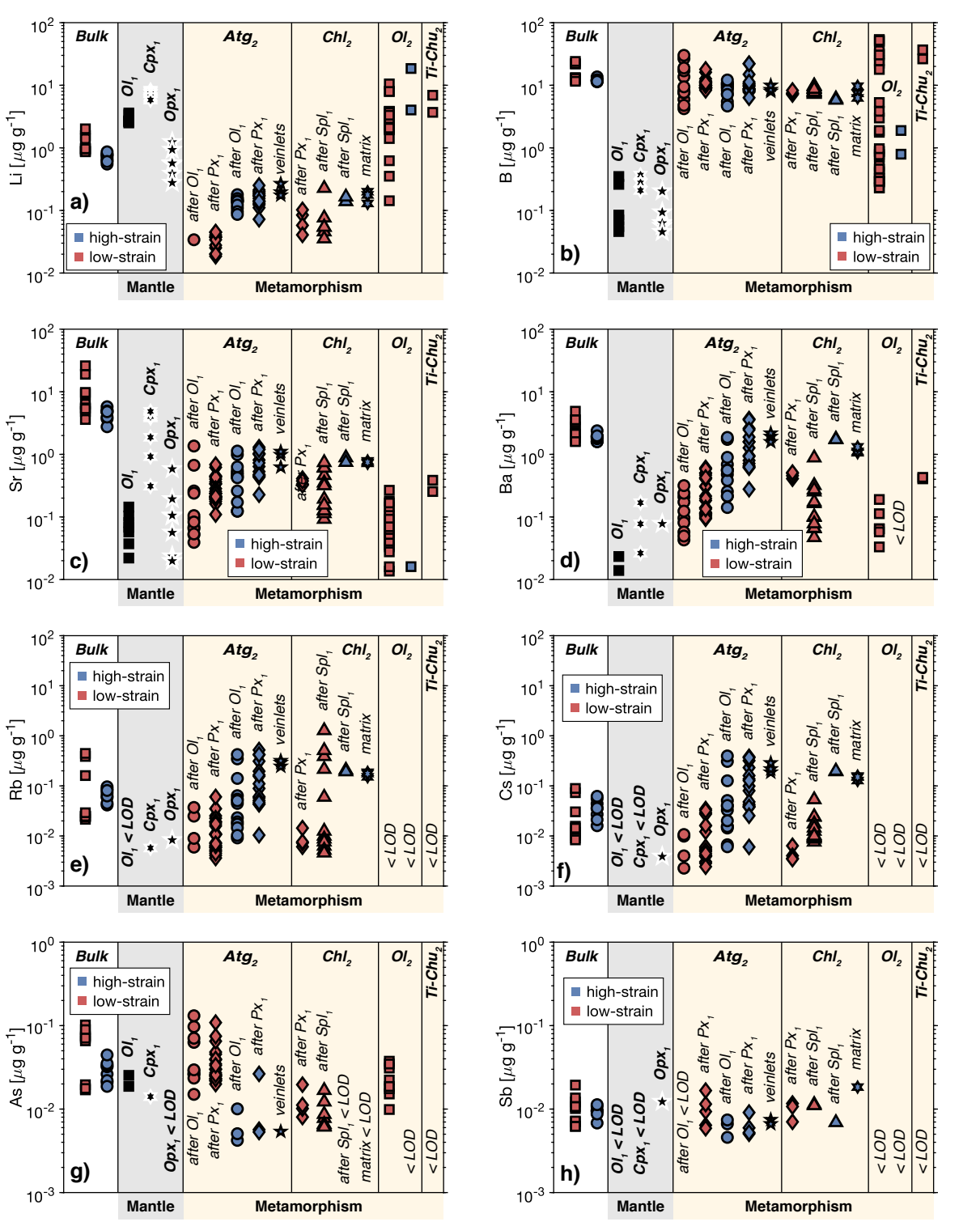
a)
Li [μg g-1]
Bulk
Ol1
Cpx1
Opx1
Atg2
after Ol1
after Px1
after Ol1
after Px1
veinlets
Chl2
after Px1
after Spl1
after Spl1
matrix
Ol2
Ti-Chu2
high-strain
low-strain
Mantle
Metamorphism
b)
B [μg g-1]
Bulk
Ol1
Cpx1
Opx1
Atg2
after Ol1
after Px1
after Ol1
after Px1
veinlets
Chl2
after Px1
after Spl1
after Spl1
matrix
Ol2
Ti-Chu2
high-strain
low-strain
Mantle
Metamorphism
c)
Sr [μg g-1]
Bulk
Ol1
Cpx1
Opx1
Atg2
after Ol1
after Px1
after Ol1
after Px1
veinlets
Chl2
after Px1
after Spl1
after Spl1
matrix
Ol2
Ti-Chu2
high-strain
low-strain
Mantle
Metamorphism
d)
Ba [μg g-1]
Bulk
Ol1
Cpx1
Opx1
Atg2
after Ol1
after Px1
after Ol1
after Px1
veinlets
Chl2
after Px1
after Spl1
after Spl1
matrix
Ol2
< LOD
Ti-Chu2
high-strain
low-strain
Mantle
Metamorphism
e)
Rb [μg g-1]
Bulk
high-strain
low-strain
Ol1 < LOD
Cpx1
Opx1
Atg2
after Ol1
after Px1
after Ol1
after Px1
veinlets
Chl2
after Px1
after Spl1
after Spl1
matrix
Ol2
< LOD
< LOD
Ti-Chu2
< LOD
Mantle
Metamorphism
f)
Cs [μg g-1]
Bulk
high-strain
low-strain
Ol1 < LOD
Cpx1 < LOD
Opx1
Atg2
after Ol1
after Px1
after Ol1
after Px1
veinlets
Chl2
after Px1
after Spl1
after Spl1
matrix
Ol2
< LOD
< LOD
Ti-Chu2
< LOD
Mantle
Metamorphism
g)
As [μg g-1]
Bulk
high-strain
low-strain
Ol1
Cpx1
Opx1 < LOD
Atg2
after Ol1
after Px1
after Ol1
after Px1
veinlets
Chl2
after Px1
after Spl1
after Spl1 < LOD
matrix < LOD
Ol2
< LOD
< LOD
Ti-Chu2
Mantle
Metamorphism
h)
Sb [μg g-1]
Bulk
high-strain
low-strain
Ol1 < LOD
Cpx1 < LOD
Opx1
Atg2
after Ol1 < LOD
after Px1
after Ol1
after Px1
veinlets
Chl2
after Px1
after Spl1
after Spl1
matrix
Ol2
< LOD
< LOD
Ti-Chu2
< LOD
Mantle
Metamorphism

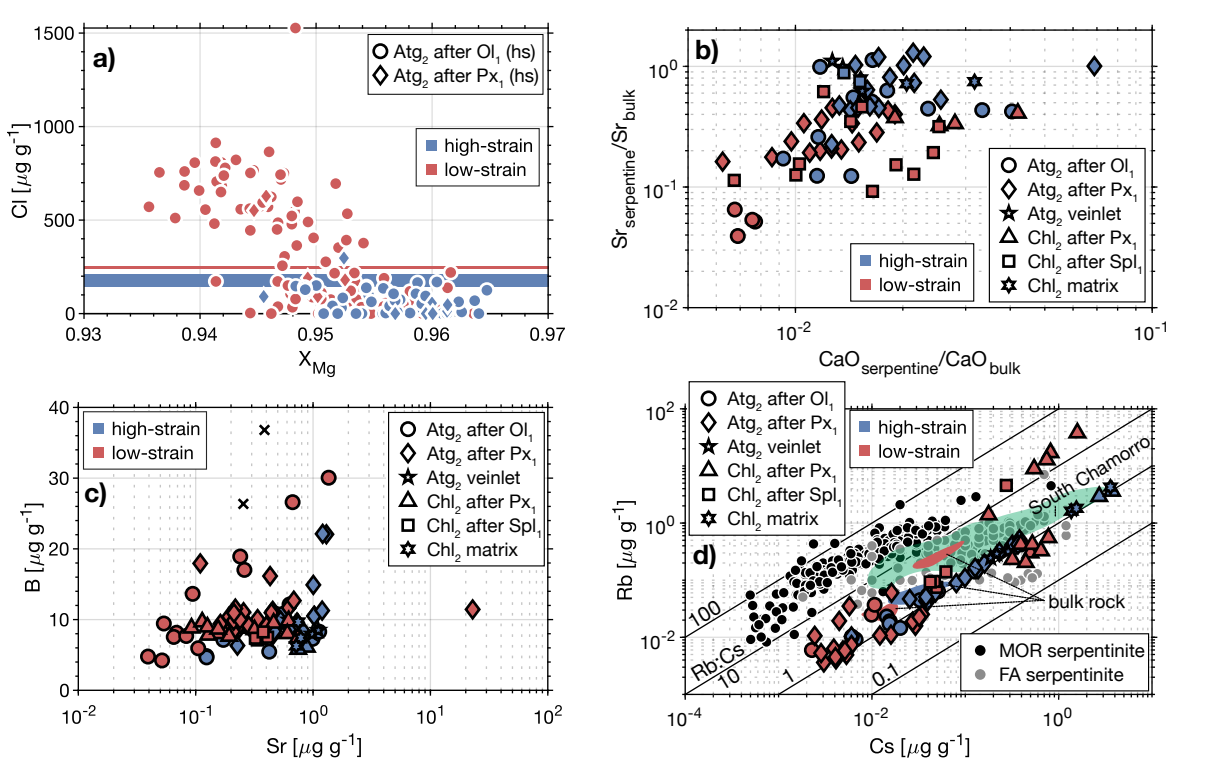
a)
Atg2 after Ol1 (hs)
Atg2 after Px1 (hs)
high-strain
low-strain
Cl [μg g-1]
XMg
b)
Srserpentine/Srbulk
CaOserpentine/CaObulk
Atg2 after Ol1
Atg2 after Px1
Atg2 veinlet
Chl2 after Px1
Chl2 after Spl1
Chl2 matrix
high-strain
low-strain
c)
B [μg g-1]
Sr [μg g-1]
d)
Rb [μg g-1]
Cs [μg g-1]
South Chamorro
bulk rock
Rb:Cs
100
10
1
0.1
MOR serpentinite
FA serpentinite

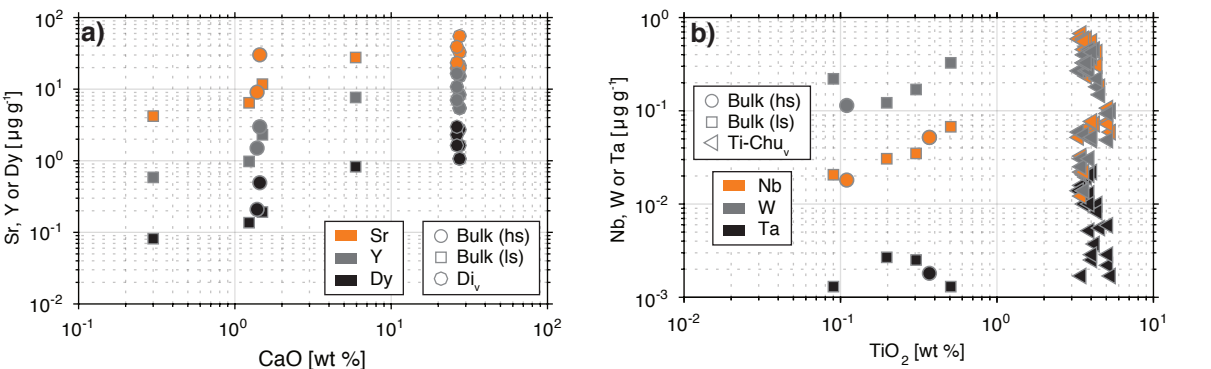
a)
Sr, Y or Dy [µg g-1]
CaO [wt %]
Sr
Y
Dy
Bulk (hs)
Bulk (ls)
Div
b)
Nb, W or Ta [µg g-1]
TiO2 [wt %]
Bulk (hs)
Bulk (ls)
Ti-Chuv
Nb
W
Ta

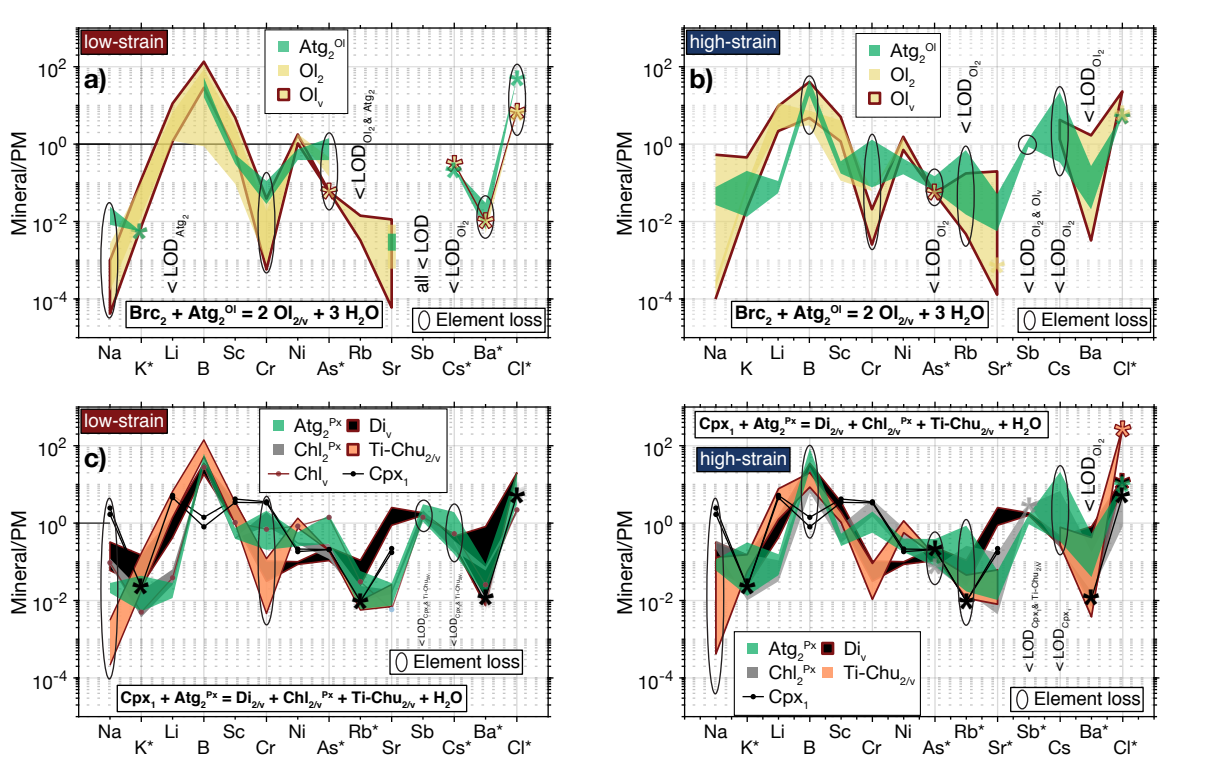
low-strain
a)
Atg2Ol
Ol2
Olv
Mineral/PM
< LODAtg2
< LODOl2 & Atg2
all < LOD
< LODOl2
Brc2 + Atg2Ol = 2 Ol2/v + 3 H2O
Element loss
Na K* Li B Sc Cr Ni As* Rb Sr Sb Cs* Ba* Cl*
high-strain
b)
< LODOl2
< LODOl2 & Olv
Na K Li B Sc Cr Ni As* Rb Sr* Sb Cs Ba Cl*
low-strain
c)
Atg2Px
Di v
Chl2Px
Ti-Chu2/v
Chlv
Cpx1
Cpx1 + Atg2Px = Di2/v + Chl2/vPx + Ti-Chu2/v + H2O
Na K* Li B Sc Cr Ni As* Rb* Sr Sb Cs* Ba* Cl*
high-strain
< LODCpx1
Na K* Li B Sc Cr Ni As* Rb* Sr* Sb* Cs Ba* Cl*

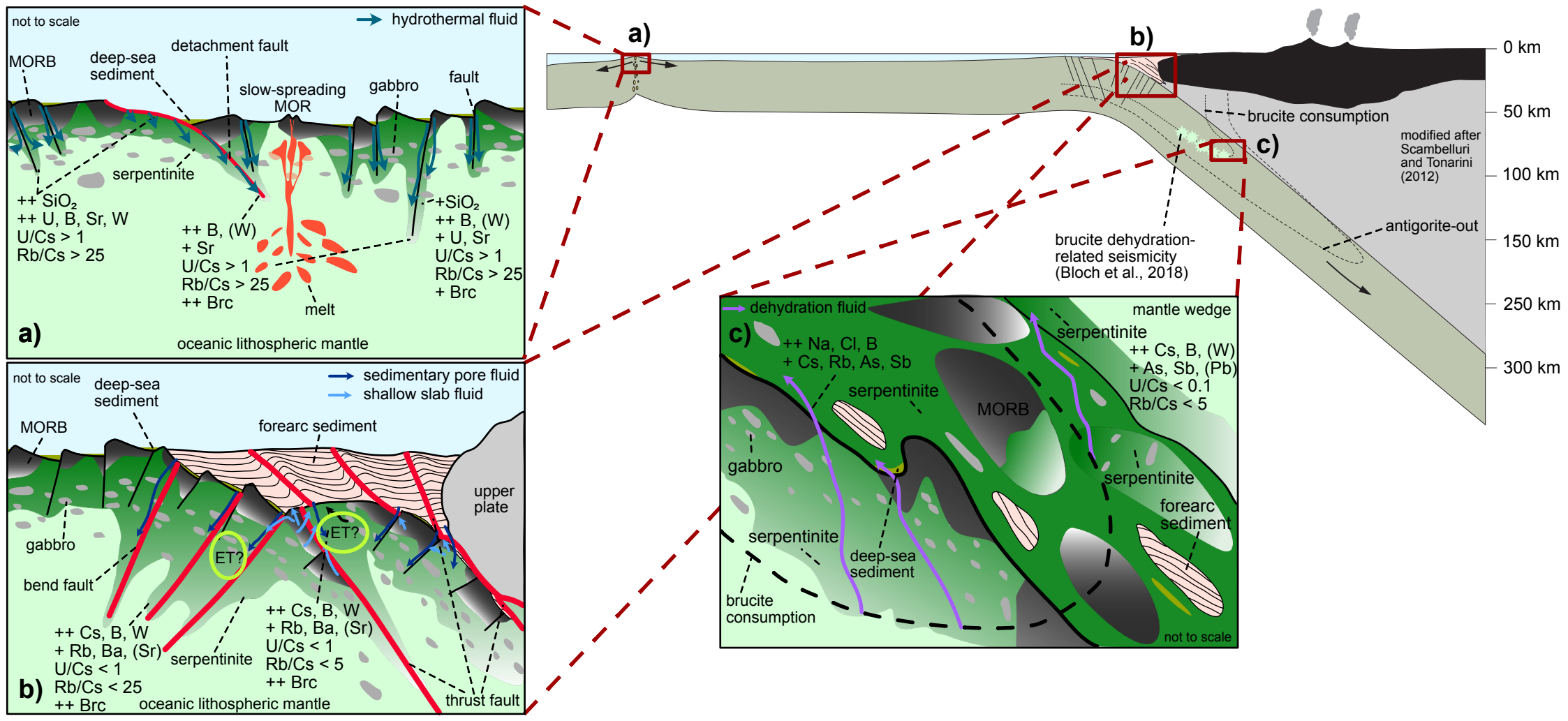
not to scale
hydrothermal fluid
MORB
deep-sea sediment
detachment fault
slow-spreading MOR
gabbro
fault
serpentinite
++ SiO2
++ U, B, Sr, W
U/Cs > 1
Rb/Cs > 25
++ B, (W)
+ Sr
U/Cs > 1
Rb/Cs > 25
++ Brc
melt
+SiO2
++ B, (W)
+ U, Sr
U/Cs > 1
Rb/Cs > 25
+ Brc
a)
oceanic lithospheric mantle
not to scale
sedimentary pore fluid
shallow slab fluid
deep-sea sediment
MORB
forearc sediment
upper plate
gabbro
bend fault
ET?
ET?
++ Cs, B, W
+ Rb, Ba, (Sr)
U/Cs < 1
Rb/Cs < 25
++ Brc
serpentinite
++ Cs, B, W
+ Rb, Ba, (Sr)
U/Cs < 1
Rb/Cs < 5
++ Brc
b)
oceanic lithospheric mantle
thrust fault
a)
b)
c)
brucite consumption
modified after Scambelluri and Tonarini (2012)
antigorite-out
brucite dehydration-related seismicity (Bloch et al., 2018)
0 km
50 km
100 km
150 km
250 km
300 km
dehydration fluid
mantle wedge
c)
++ Na, Cl, B
+ Cs, Rb, As, Sb
serpentinite
MORB
serpentinite
++ Cs, B, (W)
+ As, Sb, (Pb)
U/Cs < 0.1
Rb/Cs < 5
gabbro
serpentinite
forearc sediment
serpentinite
deep-sea sediment
brucite consumption
not to scale